



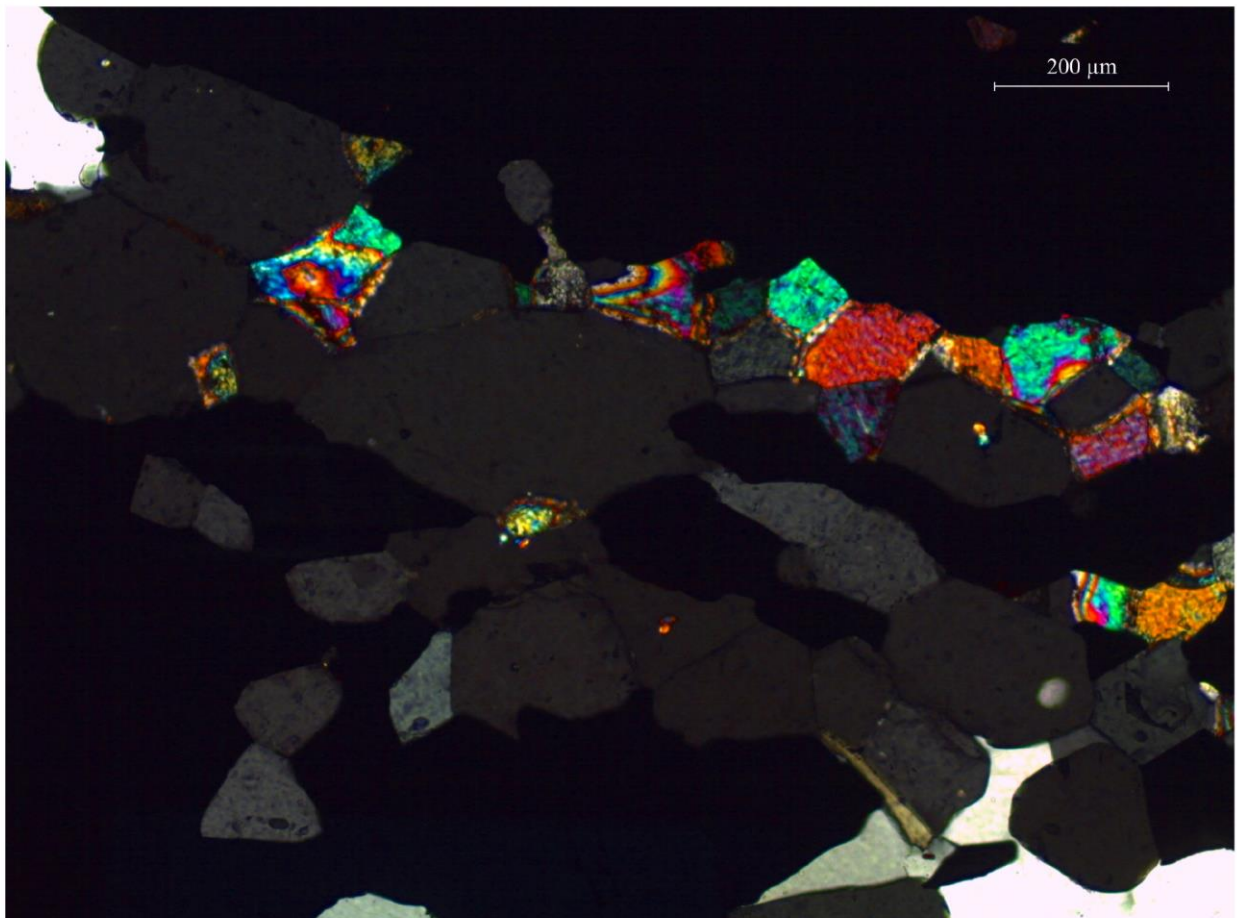
Stockholm
University

Bachelor Thesis

Degree Project in
Geology 15 hp

REE distribution and mineralogy in the Blötberget Apatite-Iron Oxide deposit; insights from the Hugget ore body

Anton Eriksson



Stockholm 2025

Department of Geological Sciences
Stockholm University
SE-106 91 Stockholm

Abstract

The transition to sustainable energy technologies is driving global demand for rare earth elements (REEs), leading an increased interest in locating sources within Europe. This study investigates REE distribution and mineralogy in a drill core from the Blötberget iron-oxide-apatite deposit, located in the Bergslagen region of south-central Sweden. The core was analysed using a combination of XCT-XRF scanning with the GeoCore X10, petrographic microscopy and SEM-EDS to characterize REE-bearing phases and evaluate the effectiveness of non-destructive scanning methods. Results show that REEs are predominantly confined to banded iron ore intervals rich in hematite and magnetite, with phosphorus serving as a reliable proxy for REE enrichment, although exceptions occur in phases such as allanite. The primary REE host minerals are monazite-(Ce) and xenotime-(Y), often associated with fluorapatite, while allanite-(Ce) appears near granitic contact zones. XCT-XRF proved effective in identifying zones of REE-enrichment but showed limitations in quantifying low-concentration phases due to matrix effects and detection limits. Comparison with assay data confirmed strong correlation for most major elements, while REEs exhibited greater variability. These findings suggest that REEs at Blötberget are largely recoverable through conventional iron ore mining. The study supports integrating XCT-XRF with traditional analytical methods for early-stage REE exploration and highlights the value of the Blötberget deposit in supporting European REE independence.

Contents

Abstract	2
1. Introduction	5
2. Aims and Hypothesis	7
2.1 Aims.....	7
2.2 Hypothesis	8
3. Geological setting.....	8
3.1 Geology of Bergslagen	8
3.2 Kiruna-type IOA.....	9
3.3 Blötberget.....	10
4. Methods	12
4.1 Core scanning.....	12
4.2 Core logging.....	14
4.3 Petrographic microscopy	14
4.4 Scanning Electron Microscopy with Energy-Dispersive X-ray Spectroscopy (SEM-EDS)	14
5. Results	15
5.1 Drill core description	15
5.2 Petrographic descriptions of main rock units	18
5.2.1 Intrusive rocks	18
5.2.2 Metavolcanic host rocks.....	20
5.2.3 Banded iron ore	26
5.3 XCT-XRF Scanning.....	32
5.4 Host minerals for REEs	35
5.4.1 Analysis from Insight.....	35
5.4.2 Analysis from SEM-EDS.....	37
5.5 Comparison between XCT-XRF and assay data	42
6. Discussion.....	44
6.1 Evaluation of XCT-XRF performance.....	44
6.2 REE distribution patterns	46
6.3 Host minerals for REEs	47
6.4 Implications.....	49

6.5 Suggestions for further research.....	50
7. Conclusions.....	51
8. Acknowledgements	52
9. References	53
10. APPENDIX.....	57
A: Thin sections obtained from drill core BB-14-013	57

1. Introduction

The global decarbonization effort linked to the development of technologies, such as solar panels, wind turbines, electric vehicles and batteries, is projected to dramatically increase global demand for critical minerals and metals such as cobalt, copper, lithium and rare earth elements (REEs) (e.g., Goodenough et al., 2016; Sovacool et al., 2020). The REEs is a group consisting of 17 chemically similar elements known as the lanthanide's series together with scandium and yttrium according to the International Union of Pure and Applied Chemistry (IUPAC) (Connelly et al., 2005). The REEs have applications in technological components such as magnets, catalysts, electronics, optics as well as in medicine and are considered part of the sustainable and low-carbon dioxide transition (Goodenough et al., 2016). As of today, and for the last decades the supply chain is largely under a global monopoly, where China stands for the majority of global production (Mancheri, 2012). Europe is increasingly focused on changing its approach to lessen reliance on geographically and geopolitically constrained supply chains (Chen et al., 2024; Goodenough et al., 2016) and in 2023 the European Commission proposed the Critical Raw Materials Act (CRMA) to implement this (European Commission 2023). Joint projects like EURARE and ASTER, with the aim to assess potential and develop new efficient and sustainable European REE ore, are carried out with the intention to build up a European industry (Bobba et al., 2020; Goodenough et al., 2016).

A wide range of REE deposits have been identified across Europe, with the Fennoscandian Shield in northern Europe and its overlying units considered among the most promising targets for future exploration (e.g., Goodenough et al. 2016). On 25 March 2025, the European Commission (2025) gave its official approval to several selected strategic projects under the CRMA, including two REE projects in Kiruna, northern Sweden, led by LKAB (Luossavaara-Kiirunavaara AB).

A similar type of deposit to Kiruna within this region is the historically active mining province of Bergslagen in south-central Sweden and it is notable for its rich variety of minerals (Ripa & Kübler, 2003). The mineralization in Bergslagen is mainly hosted in Svecofennian metavolcanic rocks and consists of two primary styles: iron oxide-apatite (IOA) deposits (e.g., Grängesberg, Blötberget) and polymetallic magnetite-skarn mineralization (Bastnäs). The area offers a wide range of variable rock types but the mineralization in both cases occur in layered stratigraphy.

Blötberget is the second largest and productive iron ore field in south-central Sweden after its close neighbour, Grängesberg mining district. Its two mines stopped production in 1979 due to a reduced demand and production in European iron mining during the late 1900s.

However, plans are now underway to reopen the Blötberget mine for iron ore extraction by the company Nordic Iron Ore AB. There is also an interest in determining the potential to mine REEs as a by-product. Despite its classification as a classic IOA deposit, limited information is available on its geological characteristics and rare earth element distribution. The mineralization in the area is dominantly composed of magnetite and hematite, with fluorapatite as the key non-oxide phase (Jonsson et al., 2016; Jiao, 2011).

Apatite incorporates REE's through substitution for Ca^{2+} and are considered the significant role in controlling REE distribution in IOA ores (Frietsch & Perdahl 1995).

While the enriched REE-bearing minerals, fluorapatite together with monazite, xenotime, and allanite are identified in the deposit (Jiao, 2011), detailed knowledge of the extent and distribution REE mineralization in different ore bodies within the Blötberget deposit is limited, especially over large areas such as the length of a drill core.

This study will utilize the Geocore X10 scanner, developed by Orexplore Solutions AB, to produce 3D compositional imaging of a drill core using integrated XCT and XRF technologies to evaluate its effectiveness for this type of ore deposit and study.

Approximately 60 meters of core was scanned and analysed using Orexplore Insight software to identify the texture, distribution and mineral signatures of REE-bearing phases. The investigated core, BB-14-013, is recovered from the intermediate depth extension of the Hugget ore body. It is located in the northeastern part of Blötberget deposit which is primarily composed of magnetite and hematite within a metavolcanic stratigraphy.

Preliminary core logging has been conducted and geochemical assays for some of the core have been provided by Nordic Iron Ore, including phosphorus concentrations which are generally thought to act as a proxy for REEs (Jiao, 2011). Selected samples from the drill core were made into thin sections, and the results from the Geocore X10 scanner were compared and validated through petrographic and SEM-EDS analysis together with comparison with the chemical assays.

2. Aims and Hypothesis

2.1 Aims

The aim for this project was to investigate the distribution of REE mineralisation within a mineralised drill core and to identify the minerals hosting the REE's. The project seeks to enhance our understanding of IOA mineralization at Blötberget by integrating drill core scanning technology with geochemical and mineralogical data. The study aims to evaluate whether specific styles of ore (i.e. magnetite vs hematite dominated) or specific locations within the ore bodies (i.e. margins or Fe oxide layers) are more enriched in REE's and should be strategically targeted to extract the REEs.

2.2 Hypothesis

- Integrating core scanning data with geochemical and mineralogical analysis can effectively identify REE-bearing phases in the Blötberget deposit and assess their recoverability during iron ore mining.

3. Geological setting

3.1 Geology of Bergslagen

The magmatic and diversly mineralized region of Bergslagen is part of the Svekokarelian orogen within the Fennoscandian Shield (Stephens & Jansson, 2020). It consists of a complex assemblage of ca. 1.91- 1.87 Ga metavolcanic and metasedimentary supracrustal rocks, primarily felsic to intermediate in composition, intruded by multiple generations of granitoid rocks (Allen et al., 1996). These rocks have been subjected to multiple phases of deformation and metamorphism with exposed rocks ranging in grades from greenschist to upper amphibolite facies.

The volcanic rocks are dominantly calc-alkaline rhyolites and dacites, interpreted to have been formed as part of an extensional back-arc caldera complex close to a continental margin (Allen et al., 1996). Volcaniclastic units, such as fine-grained ash-siltstones, are interlayered with carbonate rocks (metalimestones), many of which are hydrothermally altered and locally mineralized. The stratigraphy reflects deposition in subaerial to shallow marine environments, with ore formation related to the waning stages of volcanism and hydrothermal activity (Allen et al., 1996).

Bergslagen hosts a diverse range of mineral deposits, including skarn-hosted Fe and Fe-Mn oxides, quartz-banded iron formations (BIFs), Kiruna-type IOA deposits, and Zn–Pb–Ag ± Cu ± Au sulfides (Stephens & Jansson, 2020, and references therein). Although the Kiruna-

type IOA deposits are limited to a few occurrences in the northwestern part of Bergslagen, they have historically accounted for nearly half of the district's total iron production.

3.2 Kiruna-type IOA

The type locality for Kiruna-type IOA deposits is the Kiirunavaara deposit in northern Sweden. The assemblage is composed of magnetite-hematite-apatite, where the content of P varies but is typically below 2%, hosted by Paleoproterozoic rocks (Frietsch & Perdahl 1995). The apatite in the Kiruna iron ores contains between 1250-6700 ppm REEs.

Kiruna-type IOA deposits are also a key group in Bergslagen, typically hosted in subvolcanic intrusions. They are characterized by iron oxides appearing as massive ore bodies, in veins and disseminated in the host rock together with high concentrations of apatite (0.5-1.3 wt% P), with little evidence of sedimentary precursors or skarn development (Stephens & Jansson, 2020).

While there is an ongoing discussion on the genetic formation of IOA deposits, interpretations from modern studies from Bergslagen area favour that these have formed by an intrusive-magmatic or high-temperature, magmatic-hydrothermal process (Allen et al., 1996; Jonsson et al., 2013). Their spatial association with volcanic centres supports a genesis linked to volatile-rich melts and late-stage fluid evolution (Stephens & Jansson, 2020; Allen et al., 1996).

3.3 Blötberget

Blötberget area is located in the northwestern part of Bergslagen, near the city of Ludvika (Fig. 1). The deposits are situated within 1.90-1.87 Ga felsic to intermediate metavolcanic rocks that were later subjected to deformation and metamorphism under low-pressure amphibolite facies conditions during the Svecokarelian orogenic event (Allen et al. 1996; Stephens et al. 2009). It is classified as a Kiruna-type IOA deposit, characterized by magnetite and hematite as the primary iron-bearing minerals, with a significant apatite content contributing to the phosphorus grade (Stephens et al., 2009). Historic production at Blötberget reached 43.7 Mt at average grades of 60% Fe and 0.7% P (Allen et al., 1996).

Geographically, the mineralized zone at Blötberget follows a northeast-southwest trend, inferred from regional aeromagnetic anomalies (Almqvist et al., 2019). The mineralized bodies occur as a series of five vertically narrow, elongated lenses dipping at an angle of 50° to 70° toward the southeast (Fig. 2). These lenses are named Kalvgruvan, Flygruvan, Hugget, Betsta (also referred to as “The Wedge”), and Sandell (DMT, 2015). Geophysical surveys and historical drillhole data suggest that the mineralization extends to depths of at least 900 m below surface (DMT, 2015). In 2014, a drilling program was initiated to investigate the intermediate depth extension of the Hugget area, targeting depths between 320 m and 660 m (DMT, 2015). Drill core BB-14-013, which forms the basis of this study, was recovered during this campaign and spans a depth interval from 520.0 m to 582.6 m (Fig. 2).

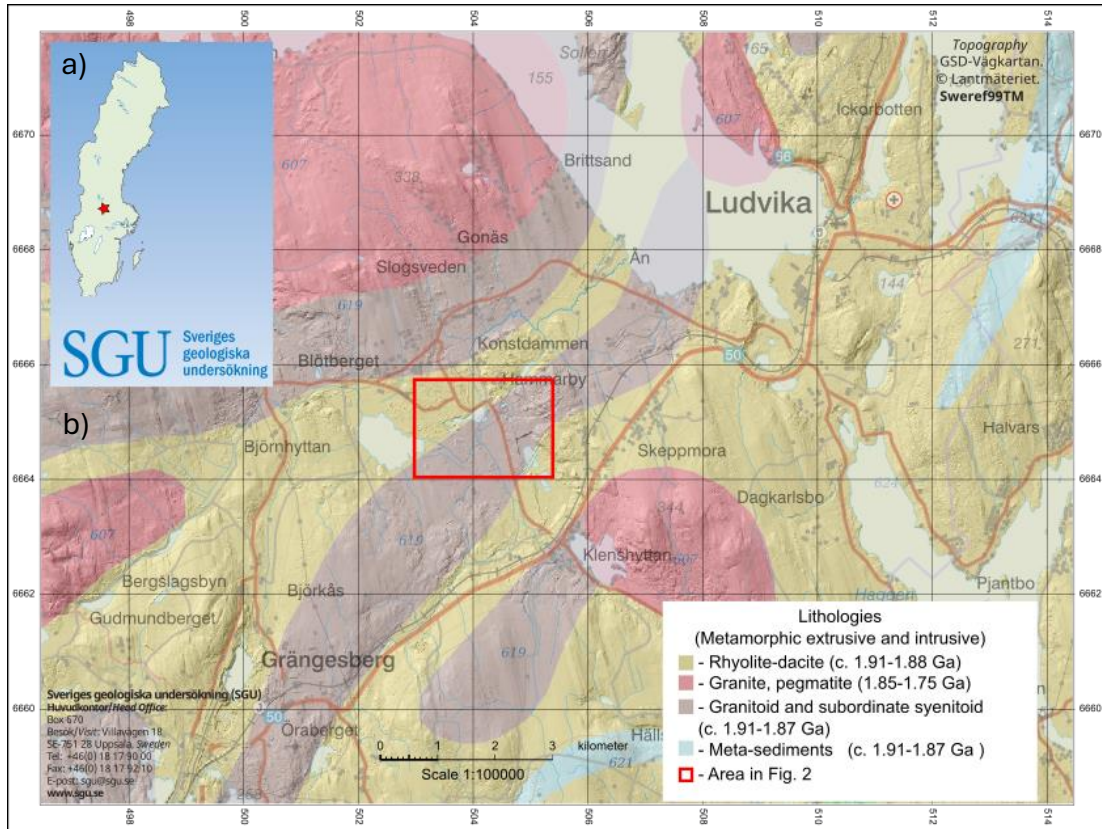


Figure 1a-b. a) Outline map of Sweden, with the study area indicated by a red star. b) Geological map of the study area. The Blötberget deposits indicated by red square (area in Fig.2). (Modified from SGU Bedrock 1:1 million, SWEREF 99TM)

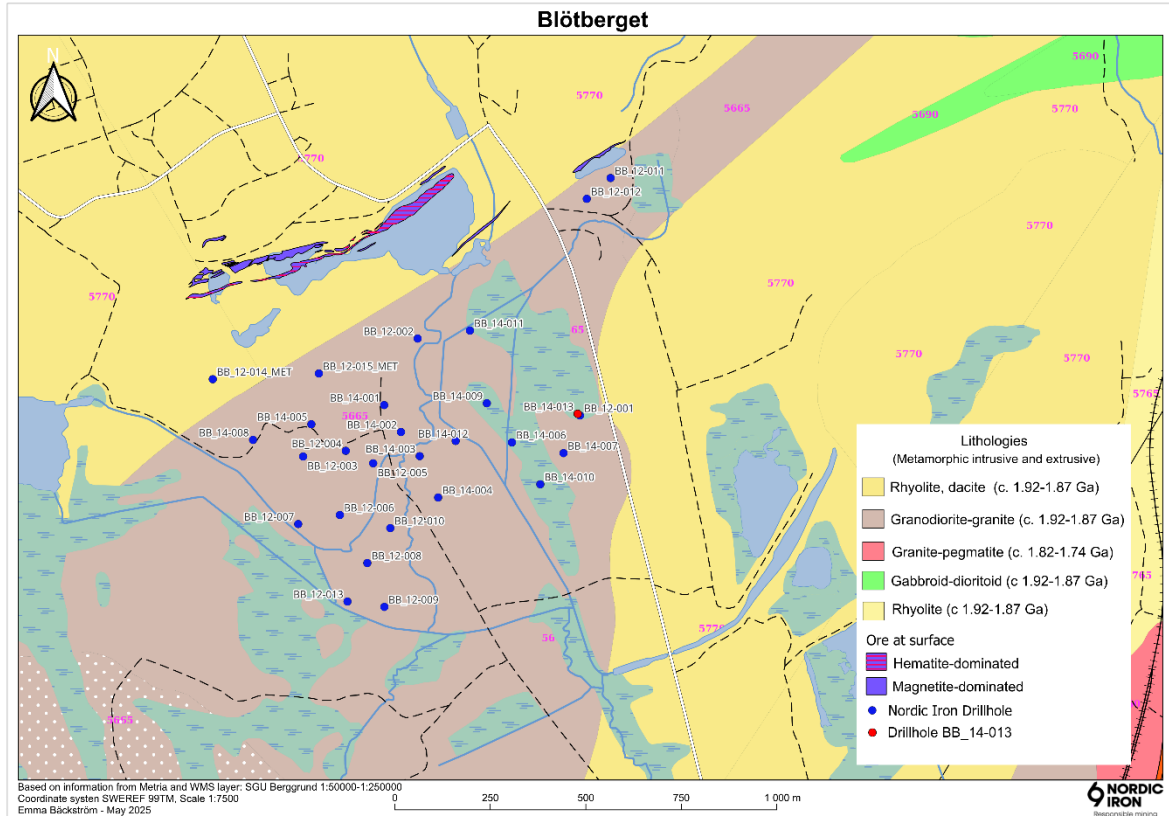


Figure 2. Map from Blötberget deposits with location of the drill hole BB-14-013, subject for this study (area is highlighted by red square in Fig.1). (Modified from NORDIC IRON, SWEREF 99TM)

4. Methods

4.1 Core scanning

The drill core BB-14-013, consisting of both half and full core, was scanned between 520m and 577m depths using the GeoCore X10 (hereafter referred to as ‘the scanner’) developed by Orexplore Solutions AB. The GeoCore X10 is a non-destructive digital assay instrument that combines X-ray computed tomography (XCT) scanning technology and X-ray fluorescence (XRF) chemical analyses to provide in-depth analysis of chemical composition and rock and mineral texture in rock drill cores. Through the accompanying software Orexplore Insight, the scanning-data is imported and organised and shown in digital detail. Together with an interactive 3D view of the core, element concentrations can be targeted and compared throughout the analysed core or in manually selected segments down to 8mm in thickness.

The GeoCore X10 uses a tungsten anode X-ray source with a 50 µm focal spot, a 100 µm pixel transmission detector, and a spectrometer, all vertically mobile during scanning as the drill core rotates (Luth et al., 2022). Up to four separate one-meter core sections are loaded into carbon fibre reinforced epoxy tubes that are placed vertically inside the instrument. The tubes are perforated to allow the X-ray signal to reach the drill core surface unobstructed. The scanning time can be adjusted from 1-6 m per hour depending on the precision on signal/noise ratio. For this survey the drill core was scanned using the rate 4 m/h together with an X-ray energy of 120 kVp to produce a 3D image result with a 200 µm resolution per voxel side.

The XCT scanning provides an attenuation measurement in the drill core which is closely related to the material’s density and average atomic weight. Materials with greater density

and heavier atomic weight exhibit higher attenuation, making them more resistant to X-rays. For example, dense substances like iron oxides attenuate X-rays more effectively than lighter materials such as quartz. Attenuation values are thus closely linked with mineralogy, however, as minerals exhibit compositional variability, attenuation ranges may vary between impurities and mineralogical end-members (Hansson et al., 2024). A precompiled dataset of minerals representative of the Blötberget deposit was used to match measured attenuation values to established reference values for individual minerals. Using a best-fit model helps reduce the difficulties that arise when analysing rock samples that are not uniform in composition, like a drill core spanning over different lithologies.

The XRF analysis measure the chemical composition of the surface of the drill core, and this is combined with the attenuation value to give a modelled concentration and element abundance in weight percent or parts per million values of the 3D volume (Luth et al., 2022). XRF detection limits of the GeoCore X10 are similar to traditional XRF instruments, where light elements are difficult to measure while heavier are reasonably well-analysed (Laperche & Lemièrè, 2020). The instrument approximately detects elements between atomic numbers 13 and 92 at between 10 to 100 ppm precision, while elements with atomic mass < 13 are not directly measured but are instead estimated using stoichiometric calculations (Alexander Hansson, *pers comm.*). For the XCT data there are negative physical effects such as beam hardening, photon starvation and scattered radiation which affect X-rays passing through massive metallic ore, masking internal rock features and showing artifacts in the resulting image (Kyle & Ketcham, 2015; Luth et al., 2022). The GeoCore X10 uses a photon-counting cathodoluminescence type camera to partly overcome these artifacts (Willeminck et al., 2018).

4.2 Core logging

The drill core BB-14-013 was physically logged by project supervisor Dr Iain Pitcairn, Department of Geological Sciences, Stockholm University. This log was thereafter used as the basis for digitizing the core and identifying each lithological unit along with its corresponding extent.

4.3 Petrographic microscopy

Petrographic microscopy was used to examine and identify minerals and rock types in thin sections approximately 30 μm thick. Polarized transmitted light reveals key optical properties, such as birefringence, pleochroism, and interference colours, essential for mineral identification and the interpretation of rock textures. Reflected light microscopy, using polished surfaces, was also employed to study opaque minerals, revealing colour, texture, reflectivity and anisotropy, critical for identifying ore minerals. 19 rock samples (see appendix A) were selected and made into thin sections at Thin Section Labs, Nancy, France.

4.4 Scanning Electron Microscopy with Energy-Dispersive X-ray Spectroscopy (SEM-EDS)

SEM-EDS analysis was performed at the geological laboratory of the Swedish Museum of Natural History (Naturhistoriska riksmuseet) in Stockholm. The purpose of the analysis was to investigate the mineralogical and elemental composition of seven selected thin sections (see Appendix A), to ground truth the data received from the core scanning (XCT-XRF) and petrography. The SEM provides high-resolution imaging of sample surfaces using a focused electron beam, while the EDS system identifies elemental composition based on the detection of characteristic X-rays emitted from the sample (Goldstein et al., 2017). The analysis was conducted under high vacuum conditions and with an accelerating voltage of 20kV. Instrument calibration was performed using a cobalt standard. Prior to analysis, all samples were carbon-coated to ensure conductivity.

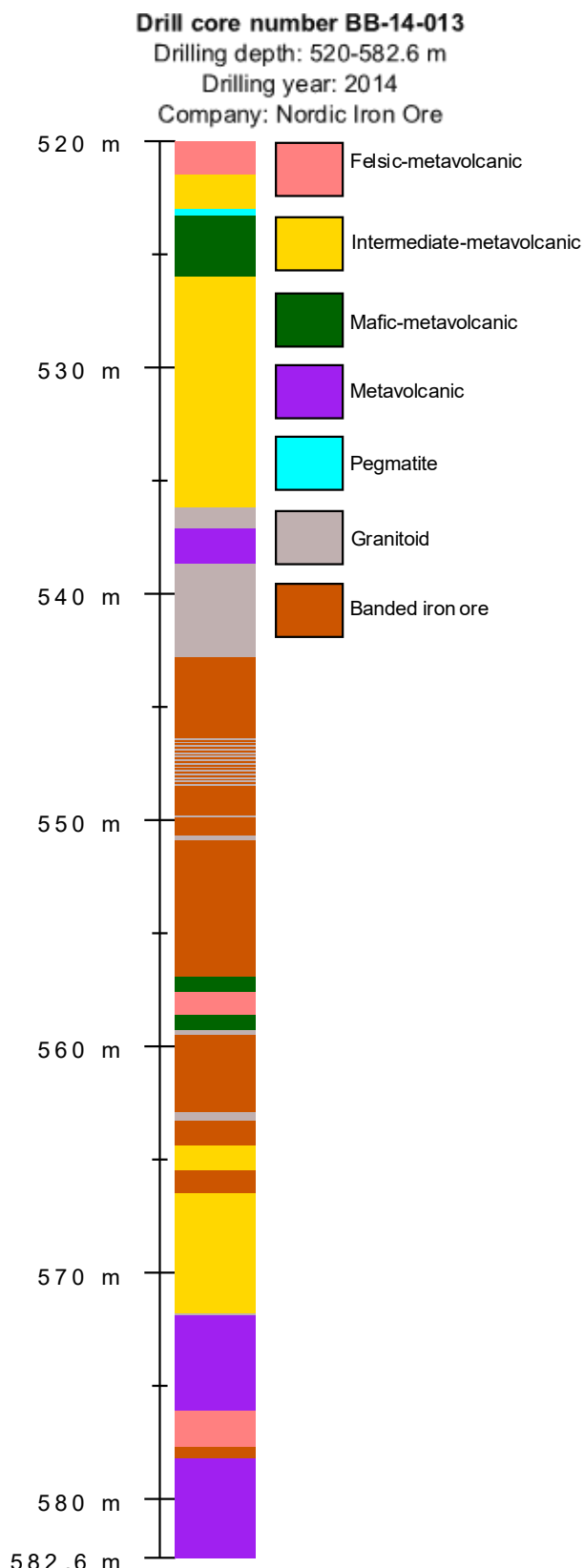


Figure 3. Drill core outline and legend showing generalized lithologies for BB-14-013 based on physical core logging. The core was drilled in the year 2014 by the company Nordic Iron Ore AB. Core depth from 520.0 m – 582.6 m.

5. Results

5.1 Drill core description

Fig. 3 shows a simplified log of rock units in drill core BB-14-013 based on the core logging made by Dr. Iain Pitcairn. Drillhole BB-14-013 intersects a sequence of predominantly metavolcanic rocks between 520.0 m and 582.6 m depth. The lithologies include felsic-metavolcanics (FMV), intermediate-metavolcanics (IMV), mafic-metavolcanics (MMV) and unspecified general metavolcanics (MV), occasionally intruded by granites and pegmatites. The metavolcanic units are termed metavolcanic based on their appearance and comparison to other areas in Bergslagen where volcanic textures and phenocrysts are present. They are generally foliated and locally banded; the foliation is primarily defined by biotite. Several sections, mainly toward the middle of the drill core, exhibit a high content of magnetite and hematite, locally banded and elsewhere more massive in character, recorded as banded iron ore (BIO). These

intervals represent the most distinct and extensive mineralized zones within the core, hereafter termed the main ore body.

The core begins at 520.0 m with banded FMV, described as fine-grained with a light pink color, gradually grading into IMV at 521.5 m. Between 521.5-526.0 m, the units are characterized by strong foliation based on biotite with varying content, scattered magnetite mineralization, and is bottomed out by a darker MMV unit with amphibole. At 523.0 m a thin vein (~30.0 cm) of pegmatite crosscut the sequence parallel to foliation.

From 526.0 to 542.8, the core is dominated by IMV and MV rocks, interspersed with granitoid intervals. The metavolcanic units are banded and foliated, containing quartz, biotite and feldspars but without any clear phenocrysts preserved. In places the more felsic units show somewhat diffuse grain boundaries and locally show red staining, presumably due to oxidation of Fe. Starting at 537.1 m, a short interval of metavolcanic rock displays chaotic gneissic texture with variable foliation. Minor magnetite and hematite are present through parts of this interval, though the iron oxide content increase significantly below this section. The granitoid unit, which ends at 542.8 m just above the BIO, gradually shows darker magnetite banding and some coarse bands of hematite toward its lower contact.

The interval from 542.8 m to 570.0 m shows a sequence dominated by BIO, interlayered with occasional granitoid intrusions and minor FMV, IMV and MMV rocks. This section of the core contains the most extensive and visually distinct mineralized zone, characterized by the presence of magnetite and hematite in varying proportions, and is considered the main ore body. Starting at 542.8 m a massive BIO unit is encountered, containing an estimated 30% magnetite and 60% hematite, with distinct brownish-grey and light-grey banding. Between

542.8 m and 557.0, multiple thick intervals of BIO are logged, often with finely alternating bands of magnetite and hematite. Some segments, such as at 548.5, are exceptionally oxide-rich, with estimates suggesting up to 95% total Fe-oxide content. These zones are commonly intruded by thin granitoid veins (e.g. at 546.3 m and 549.8 m), which locally disrupt the banding. The granitoid veins are fine- to medium-grained and typically red-rimmed at contacts parallel to subparallel to foliation. From 557.0 m to 570.0 m the core continues to show alternating BIO and different metavolcanic units, with additional granitoid intrusions. The BIO here remains well banded, with hematite and magnetite in mixed portions, while some zones (561.3 m to 561.5 m) show almost pure hematite and others (562.7 m to 562.9) almost pure massive magnetite. The IMV unit starting at 564.4 m is dark coloured and fine grained showing greenish bands, possibly chlorite, in the upper sections and several quartz veinlets throughout.

Below 570.0 m, metavolcanic rocks with interlayered iron-oxide-bearing bands persists, gradually decreasing in iron oxide content down to the end of the core at 582.6 m. The lower sections are dominated by general metavolcanic, locally foliated, with intermittent occurrences of magnetite and smaller portions of hematite.

5.2 Petrographic descriptions of main rock units

5.2.1 Intrusive rocks

In the upper part of the drill core the only unit characterized as ‘pegmatite’ is present. It crosscut surrounding units parallel to their foliation but lacks clear foliation itself. It’s characterized by a white to slight pinkish colour and distinctly coarse grained. The coarse grains, predominantly composed of quartz and K-feldspar, exhibit somewhat diffuse grain boundaries and are locally red stained. No thin sections were selected for this unit.

At several levels in the drill core, units described as ‘granites’ are present, ranging from thin (centimetre-scale) veins to bodies several meters thick. They are dominantly equigranular and range in colour from pale grey (Fig. 4a) to distinctly red stained (Fig. 4b) at contacts with iron-ore. Within the upper section of the main ore body, a succession of banded iron ore is intruded by several veins and patches of red-stained granite. These intrusions crosscut the banding of the iron ore but are also stretched along foliation (Fig. 4c). The texture exhibits folding and, in places, forms a network-like mesh of granite. Sample B-13-548.3 highlights one of these granitic veins in contact with the iron ore (Fig. 4d and e). In this sample, quartz shows evidence of grain boundary migration, typical of recrystallization. K-feldspar grains display tartan twinning and elongated biotite grains exhibit pale to brown pleochroism and moderate birefringence. Accessory amount of muscovite is also present. The Fe-oxides consists of an approximately even mix of hematite and magnetite, with accessory amounts of apatite also present (Fig. 4e).

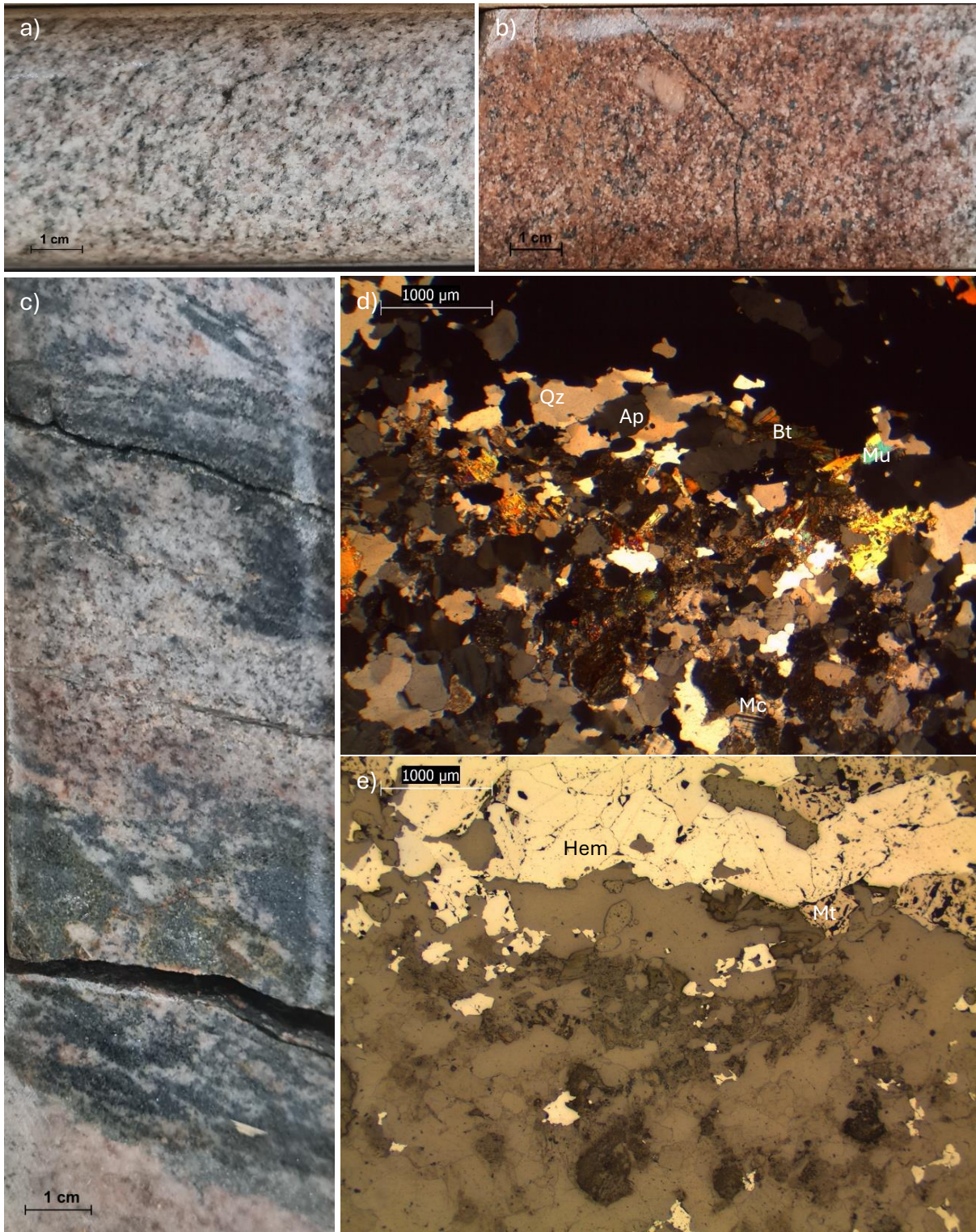


Figure 4 a-e. Three representative hand sample photos and 2 photomicrographs from intrusive units in drill core BB-14-013

a) Hand sample image of pale grey granite unit

b) Hand sample image of red stained granite unit

c) Hand sample image of a succession of banded iron ore intruded by several veins and patches of red-stained pale grey granite.

d) Sample B-13-548.3 under low magnification in XPL, showing quartz, apatite, biotite, muscovite and microcline.

e) Sample B-13-548.3 under low magnification in reflected light. Magnetite and hematite annotated.

5.2.2 Metavolcanic host rocks

The metavolcanic rocks logged in the drill core show a heterogeneous assemblage between felsic, intermediate, mafic and unspecified metavolcanic types. These rocks represent a deformed and metamorphosed sequence that is interpreted as the host rocks for the mineralization.

The felsic metavolcanic (FMV) rocks are banded consisting of massive, fine grained (0.1-0.4mm) pink quartz- and feldspar-rich layers intercalated with foliated, biotite-rich layers or patches. In some units, the FMV displays red to green bands with diffuse grain boundaries, likely due to alteration. Figure 5, showing a hand sample and a photomicrograph of sample B-13-557.9, displays elongated red grains resembling biotite in texture, but differing in colour, in a quartz and plagioclase rich FMV unit. No mineralization was observed in the FMV units.

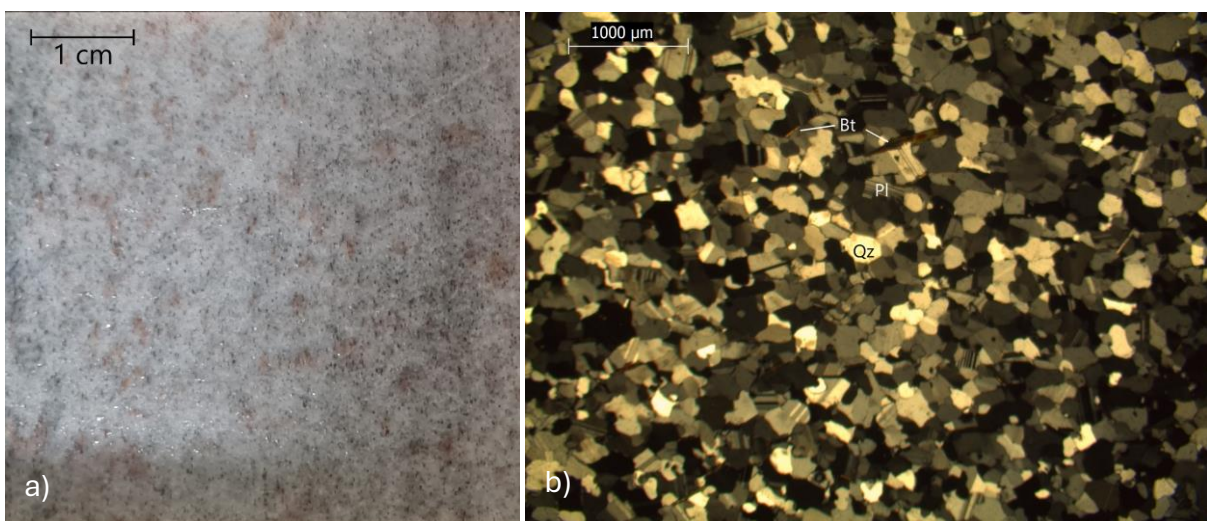


Figure 5 a-b. Hand sample photo and photomicrograph from FMV unit in drill core BB-14-013

a) Hand sample photo of FMV unit for sample B-13-557.9 at 557.9 m depth in the drill core.

b) Photomicrograph of sample B-13-557.9 under low magnification in XPL. Quartz, biotite and plagioclase annotated.

Intermediate metavolcanic (IMV) rocks are the most common rock-type both above and below the main ore body in the drill core. They are strongly foliated, with abundant biotite and quartz, and bands or patches of hematite and magnetite are present throughout most units. Sample B-13-522.5 (Fig. 6c and e) is from an IMV unit above the main ore body with a hand sample image in Figure 6a, displaying a foliation mainly defined by elongated biotite grains with domains of quartz and feldspars in between. A darker band consisting of magnetite, small amounts of pyrite and larger biotite grains is visible in the upper part of the sample (Fig. 6c and e). Slightly lower in the stratigraphy, IMV sample B-13-528.5 (Fig. 6d and f) shows foliation visible in hand sample (Fig. 6b). Mineralogically it is very similar to the unit above, with quartz and plagioclase dominating and foliation defined by biotite. The sample contains thin bands of quartz, feldspars, biotite and magnetite often with a mushy textured carbonate alteration along the edges (Fig. 6f).

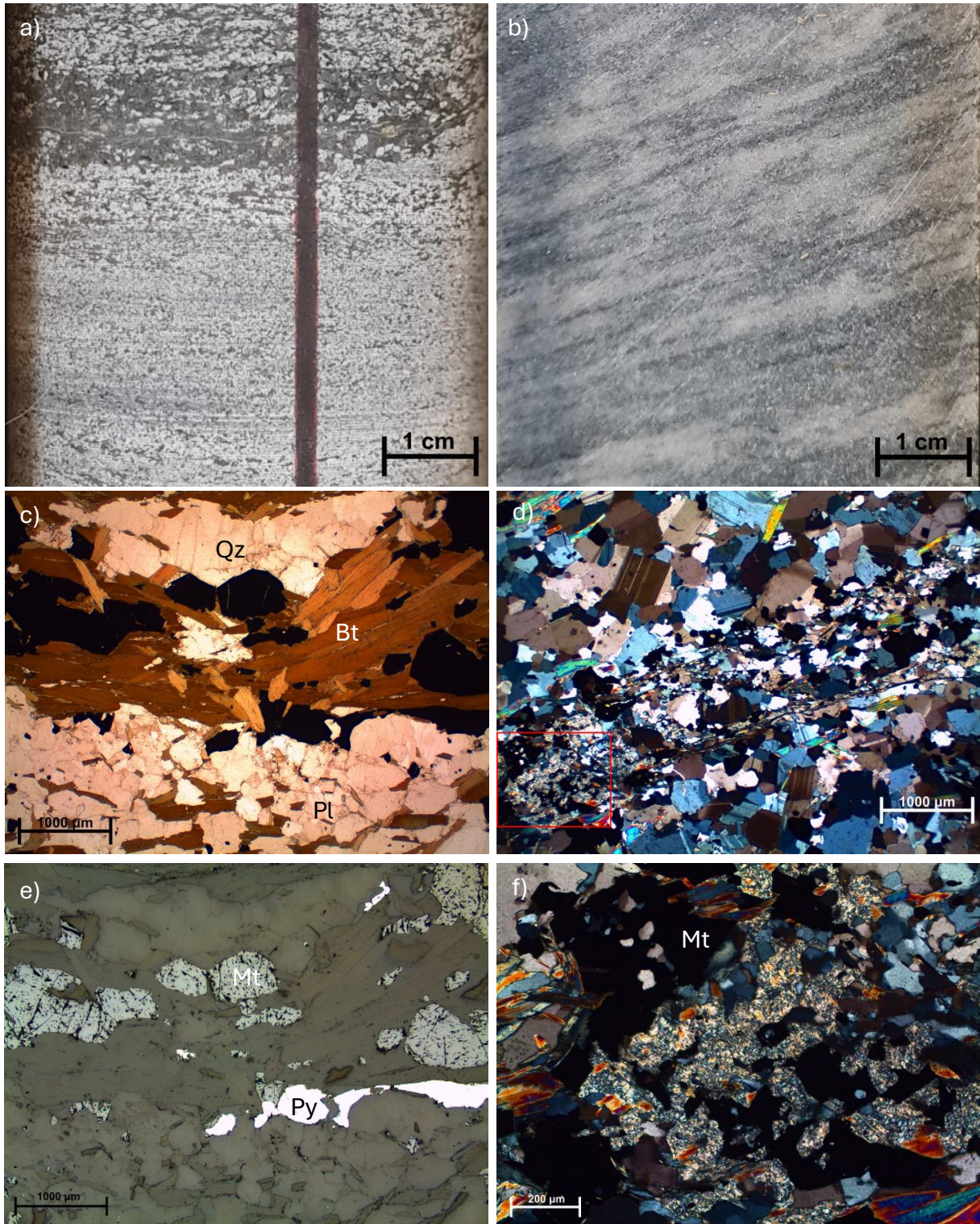


Figure 6 a-f. Two representative hand sample photos and 4 photomicrographs from IMV unit in drill core BB-14-013
a) Hand sample image IMV unit for sample B-13-522.5 at 522.5 m depth in the drill core. (The solid black line is a reference mark manually drawn on the drill core)
b) Hand sample image IMV unit for sample B-13-528.5 at 528.5 m depth in the drill core.
c) Sample B-13-522.5 under low magnification in PPL. Quartz, biotite and plagioclase annotated.
d) Sample B-13-528.5 under low magnification in XPL
e) Sample B-13-522.5, same image as (c) under low magnification in reflected light. Magnetite and pyrite annotated.
f) Sample B-13-528.5 under high magnification in XPL, area from rectangle in (d). Mushy textured carbonate alteration shown in contact with magnetite, biotite and quartz.

The mafic metavolcanics (MMV) units in the core, one present above and two in the middle of the main ore body, are massive to weakly foliated, fine-grained and distinctly darker than the other metavolcanics (Fig 7a and b). They are amphibolite units dominated by hornblende with thin layers of magnetite similar to IMV units. Patches of magnetite and sulfides also occur.

Sample B-13-525.7 (Fig. 7c and e), from the upper unit (Fig 7a), displays a fine-grained, equigranular texture dominated by hornblende, quartz and feldspars. Grain boundaries commonly show triple junctions at approximately 120° , indicating high degree of textural equilibrium. Albite, identified by its characteristic polysynthetic twinning, is the most abundant feldspar, while minor amounts of microcline displaying tartan twinning are also present. Hornblende grains show pleochroism in varying green tones and exhibit the typical cleavages at angles of about 56° and 124° (Fig. 7c and e). Disseminated iron oxides, opaque in transmitted light, occur in small amounts throughout the unit. Hematite dominates the iron oxide content, however smaller amounts of magnetite also occur.

Sample B-13-558.9 is from the middle of the main ore body. Mineralogically, it closely resembles the upper unit, except for the presence of milky white blasts with irregular shape and distribution (Fig. 7b). Under the microscope (Fig. 5d and f), these appear as altered plagioclase phenocrysts forming aggregates with a mushy texture. The aggregates contain smaller grains with high birefringence, some displaying harlequin colours. They possibly represent saussuritization, a process in which calcium-rich plagioclase alters into an assemblage of zoisite, chlorite, amphibole and carbonates.

Some units are characterized simply as metavolcanics (MV). Precise classifications were not drawn simply by their varying composition, showing textures similar to FMV, IMV and MMV and degrees in between. They are generally light to dark grey, banded and foliated, red-stained in places and dark layers of magnetite occur. No thin sections were selected for these units.

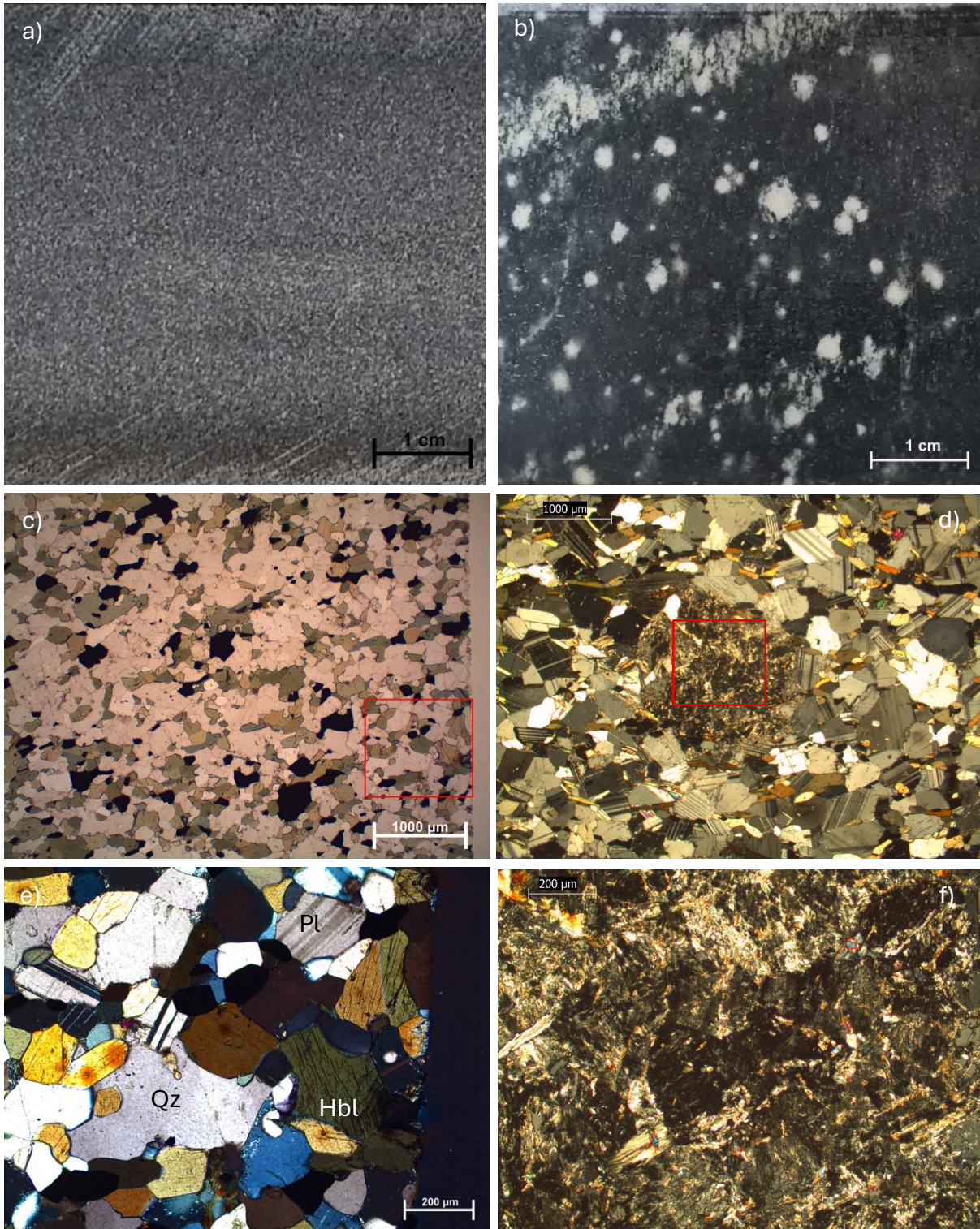


Figure 7 a-f. 2 representative hand sample photos and 4 photomicrographs from MMV unit in drill core BB-14-013.

a) Hand sample image of MMV unit for sample B-13-525.7 at 525.7 m depth in the drill core.

b) Hand sample image of MMV unit for sample B-13-528.9 at 528.9 m depth in the drill core. Image showing milky white irregular shaped and distributed blasts.

c) Sample B-13-525.7 under low magnification in PPL

d) Sample B-13-528.9 under low magnification in XPL. Image showing altered aggregate texture of the milky white blasts in (b) in the middle of image.

e) Sample B-13-525.7 under high magnification in XPL, area from rectangle in (c). Quartz, plagioclase and hornblende annotated.

f) Sample B-13-528.9 under high magnification in XPL, area from rectangle in (d). Image showing altered aggregate texture.

5.2.3 Banded iron ore

The main ore body in the core consists of rocks with intervals of massive and banded iron ore, characterized by alternating bands of iron oxide minerals with varying textures intercalated with light-coloured bands. The units display a range of mineral composition, with hematite and magnetite dominating in varying proportions. Several intervals are distinctly hematite-rich, with up to 90% iron oxides dominated by hematite, while others are magnetite-rich or demonstrate a balanced mix of both minerals. Texturally the BIO units range from massive, well banded to strongly foliated indicating structural overprints and deformation. The light-coloured, non-iron-oxide bands in the units contain quartz, accompanied with varying amounts of phosphate minerals and other accessory silicate minerals.

Sample B-13-544.2A (Fig. 8b-e), obtained from a unit located in the upper part of the main ore body (at 544.2 m depth), is dominated by massive hematite banded iron ore (Fig. 8a). The hematite grains are pale blue-grey and display strong anisotropy under reflected light. They are lath-shaped and make up more than 80% of the sample (Fig. 8d). Accessory amounts of disseminated magnetite and a single phase of pyrite are also present. Thin, light-coloured veins containing quartz, fluorapatite, and accessory minerals are observed (Fig 8b-e).

Fluorapatite appears colourless in PPL but shows distinctly higher relief relative to quartz. It occurs as euhedral, subrounded grains arranged in bands that exhibit a high degree of textural equilibrium. Smaller accessory mineral phases, characterized by very high relief and high interference colours, are concentrated within these bands, in contact with the fluorapatite grains (Fig. 8b, d and e), and are occasionally interspersed among the iron oxide phases.

These phases are identified as the REE-bearing minerals monazite and xenotime (Fig. 8e).

Monazite is clearly more abundant, while xenotime typically appears in small amounts at the edges of monazite grains.

Slightly lower in the stratigraphy, sample B-13-549.5B (Fig. 9 b-e) is from a BIO unit that is also hematite-dominant; however, magnetite is more common than in the previous sample. Magnetite appears slightly browner in reflected light and shows a pitted surface, in contrast to the smoother, more homogenous texture of hematite (Fig. 9c). Texturally, the sample exhibits alternating bands of iron oxides with thin, light-coloured veins that locally expand into larger patches, visible in hand sample (Fig. 9a). These patches consist both of euhedral, subrounded fluorapatite grains with 120-degree grain boundaries (Fig. 9b), indicating textural equilibrium, and larger, irregularly shaped fluorapatite grains containing numerous micro-inclusions (Fig. 9e and f). The micro-inclusions are predominantly monazite, although xenotime is also present.

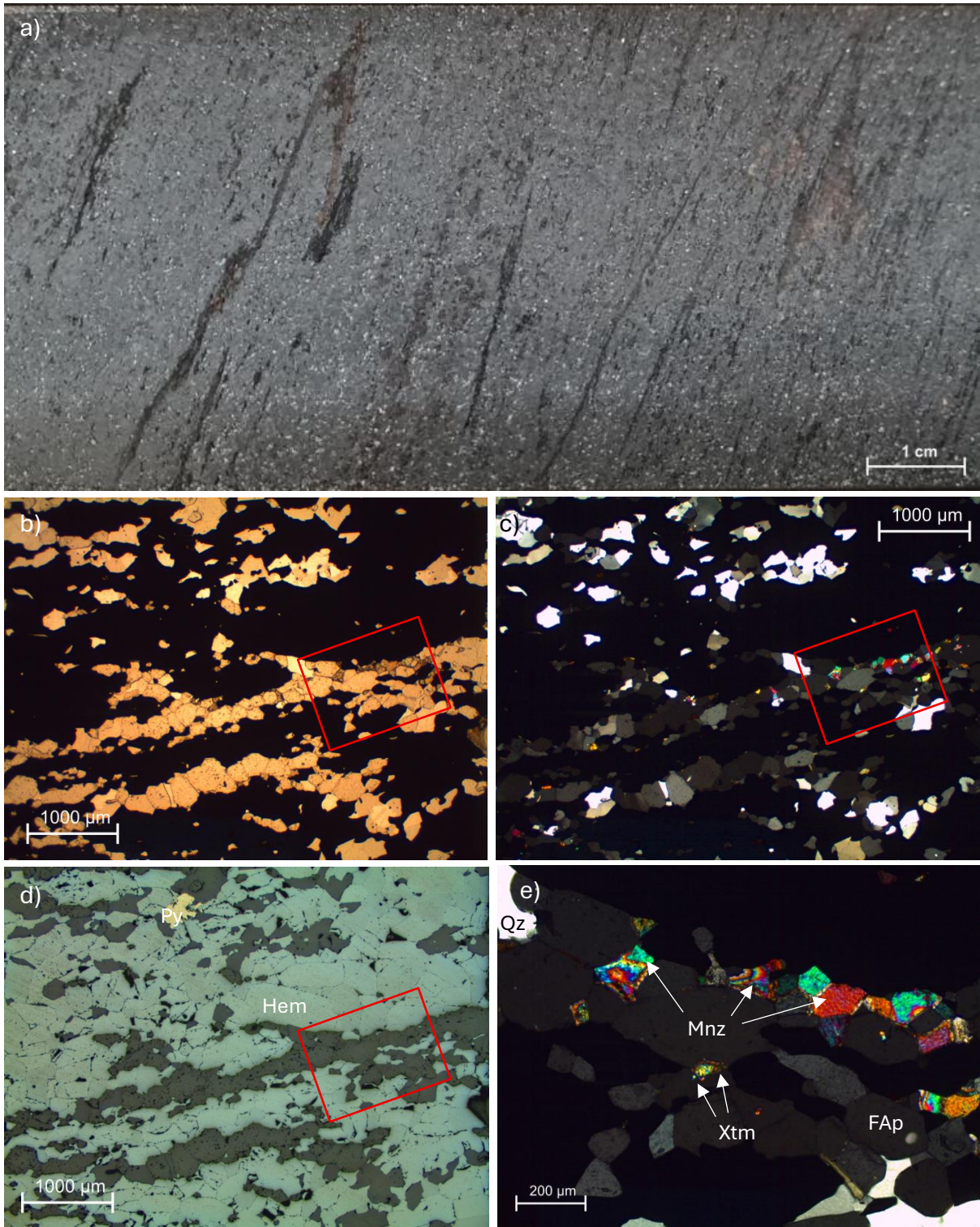


Figure 8 a-e. Representative hand sample photo and 4 photomicrographs of sample B-13-544.2A from BIO unit in drill core BB-14-013.

- a)** Hand sample image of BIO unit for sample B-13-544.2A obtained from 544.2 m depth.
- b)** Sample B-13-544.2A under low magnification in PPL (Same area as (c) and (d)).
- c)** Sample B-13-544.2A under low magnification in XPL (Same area as (b) and (d)).
- d)** Sample B-13-544.2A under low magnification in reflected light (Same area as (b) and (c)). Pyrite and hematite annotated.
- e)** Sample B-13-544.2A under high magnification in XPL, area from red rectangle in (b-d). Quartz, monazite, xenotime and fluorapatite annotated.

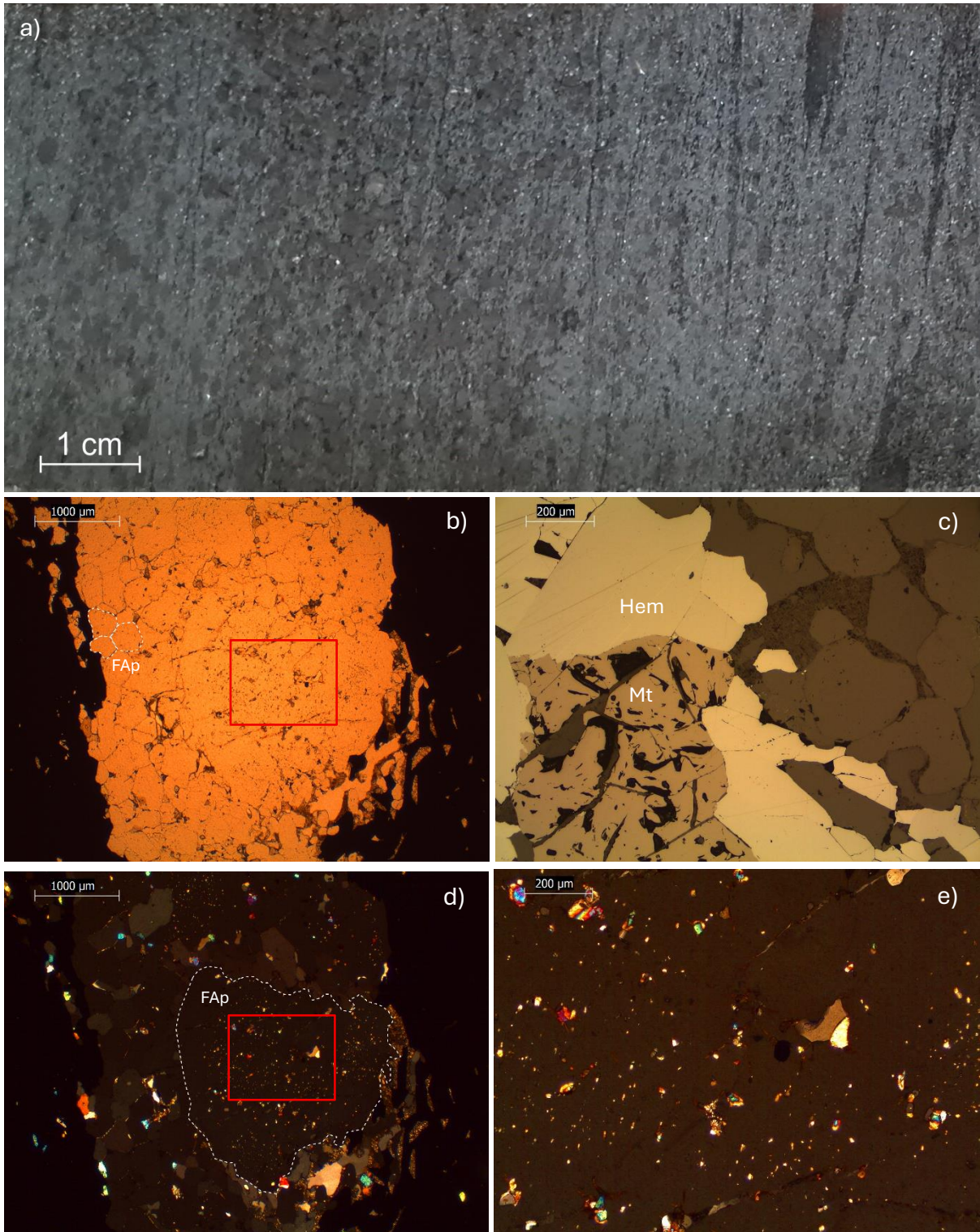


Figure 9 a-e. Representative hand sample photo and 4 photomicrographs of sample B-13-549.5B from BIO unit in drill core BB-14-013.

a) Hand sample image of BIO unit for sample B-13-549.5B at 549.5 m depth in the drill core.

b) Sample B-13-549.5B under low magnification in PPL. Showing euhedral, subrounded fluorapatite grains with 120-degree grain boundaries. Three grains highlighted with dashed white line. (Same area as (d)).

c) Sample B-13-549.5B under high magnification in in reflected light, showing hematite and magnetite.

d) Sample B-13-549.5B under low magnification in XPL. Showing irregularly shaped apatite grain, highlighted with dashed white line, containing numerous micro-inclusions. (Same area as (b)).

e) Sample B-13-549.5B under high magnification in XPL, area from red rectangle in (b) and (d). Showing micro-inclusions of monazite and xenotime.

Another BIO section in the upper part of the main ore body (at a depth of 546 m) displays a well-balanced iron-oxide assemblage, consisting of both hematite and magnetite (Fig. 10a, c). Sample B-13-546A (Fig. 10c, e) was taken from this unit and contains light-coloured bands that are dominantly composed of fluorapatite, phlogopite and allanite. The fluorapatite occurs as euhedral and subrounded grains in contact with phlogopite and allanite. The phlogopite, a Mg-rich variety of biotite, occurs as elongated grains displaying one perfect cleavage and moderate second-order interference colours (Fig. 10e). The allanite occurs as small subhedral and subrounded grains characterized by high relief, strong pleochroism, dull yellow interference colours and are often slightly zoned (Fig. 10e). Allanite is identified as a REE-bearing phase.

At several levels within the ore body of the drill core, an accessory interstitial phase occupies the space between euhedral fluorapatite grains in the light bands of the BIO units. This phase appears yellow-brown and diffusely bounded under XPL and is observed in sample B-13-560.2 (Fig. 10d, f). It is identified as a REE-bearing fluorcarbonate phase. In this sample, collected from the lower part of the ore body at 560.2 m depth (Fig. 10b), the fluorcarbonate phase occurs within fractures and in interstitial spaces between iron oxides and fluorapatite. Monazite is present both as inclusions within fluorapatite and as discrete grains embedded in the fluorcarbonate phase (Fig. 10f).

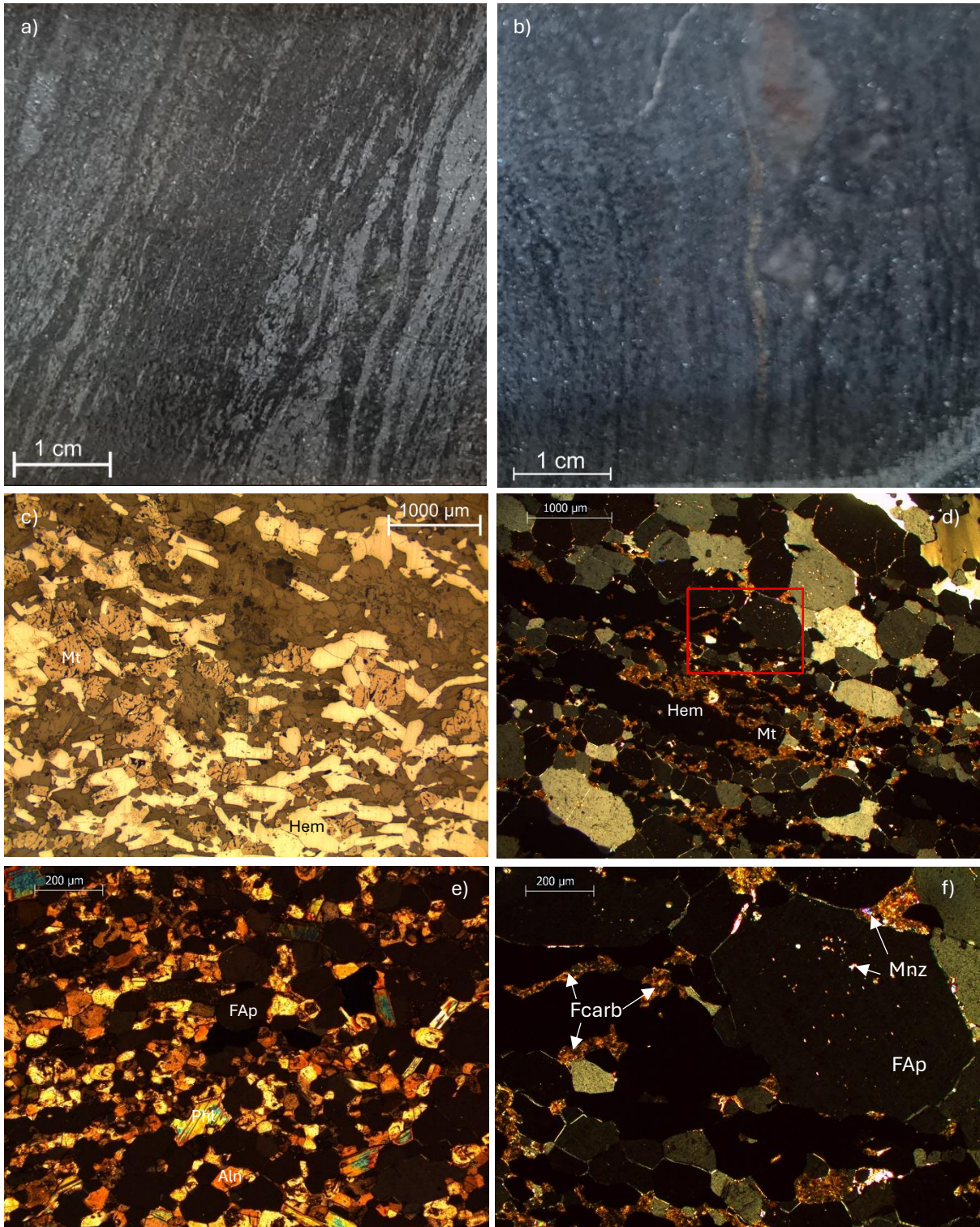


Figure 10 a-f. Representative hand sample photos and 4 photomicrographs of sample B-13-546A and B-13-560.2 from BIO unit in drill core BB-14-013.

- a)** Hand sample image of BIO unit for sample B-13-546A at 546 m depth in the drill core.
b) Hand sample image of BIO unit for sample B-13-560.2 at 560.2 m depth in the drill core.
c) Sample B-13-546A under low magnification in reflected light, showing hematite (Hem) and magnetite (Mt).
d) Sample B-13-560.2 under low magnification in XPL, showing hematite and magnetite, red square represents image (f).
e) Sample B-13-546A under high magnification in XPL. Showing phlogopite (Phl), allanite (Aln) and fluorapatite (FAp).
f) Sample B-13-560.2 under high magnification in XPL, area from red rectangle in (d). Showing fluorcarbonate (Fcarb), monazite (Mnz) and fluorapatite.

5.3 XCT-XRF Scanning

XCT-XRF scanning of the drill core reveals systematic variations in the geochemical concentrations which correspond closely with the lithological boundaries recorded in the core log (Fig. 11 and Table 1). Table 1 lists 11 units, selected to be representative parts of the drill core for this study, and their average elemental concentrations of elements that were above 0.1 wt.%. Particularly of interest for this study are the Fe, P and the combined concentrations for all detected rare earth elements (REE's). Elements such as Si and K also show trends that align with identification of lithologies during the core logging. Elevated concentrations of Si and K are observed in units logged as either felsic metavolcanics or granites, consistent with the expected composition of these rock types. While these elements are not the focus of this study, their correspondence with their rock types further supports the reliability of the XCT-XRF scanning data.

Fe concentrations are clearly high in units classified as banded iron ore (BIO), where the values range from 54.0 to 65.0 wt.% for the selected units in Table 1, as also visible in Fig. 11B. The highest concentration is observed in Unit 11 (559.5-562.9 m), which corresponds to a banded iron ore interval with highly variable magnetite to hematite ratios with minor felsic intercalations, including zones that are nearly pure hematite and others composed of almost pure magnetite. Similar but slightly lower Fe concentration is observed in Units 4, 6, 7 and 8, all logged as BIO. In contrast, metavolcanic units show lower Fe contents, typically between 6.2 and 8.8 wt.%, and as low as 0.82 wt.% for the selected FMV (Unit 9).

Phosphorus concentrations follow Fe systematically and display localized enrichment in specific BIO intervals (Fig. 11C). Unit 7 (549.9-550.7 m) contains the highest P value at 0.66 wt.%, followed by Unit 4 (542.8-546.3 m) and Unit 6 (548.5-549.8 m), with concentrations

Table 1. Elemental concentration from XCT-XRF scanning (wt%)

Unit	Lithology	Depth	Length	Si	Fe	Ca	Al	K	Na	Mg	S	Co	Ti	Zr	P	REE's (ppm)
1	IMV	521.5-523.3	1.8	31.0	6.2	1.9	4.7	2.3	na	na	0.11		0.99			171
2	MMV	523.3-526	2.7	26.0	8.5	5.8	4.6	0.76	na	na			1.5			625
3	IMV	526-535	9	33.0	7.5	1.0	4.1	1.2	na	na			0.89	0.14		18
4	BIO	542.8-546.3	3.5	5.6	56.0	3.1			na	na		0.18			0.57	2316
5	BIO/GRA	546.3-548.5	2.2	29.0	10.0	1.4	4.5	5.2	na	na			0.64			821
6	BIO	548.5-549.8	1.3	7.0	54.0	2.4	0.65	0.64	na	na		0.21			0.52	2322
7	BIO	549.9-550.7	0.8	5.6	55.0	3.3	0.27	0.3	na	na		0.20	0.17		0.66	2915
8	BIO	550.9-556.95	6.05	5.4	58.0	2.5			na	na		0.22			0.48	1135
9	FMV	557.6-558.6	1	39.0	0.98	0.7	3.4	0.68	na	na			0.13	0.12		752
10	MMV	558.6-559.3	0.7	23.0	8.8	5.6	4.9	2.0	na	na			0.72			647
11	BIO	559.5-562.9	3.4	2.0	65.0	1.7	0.12		na	na		0.20			0.36	175

Notes: blank = measured for, but below 0.1 wt.%, na = not analyzed. Depth and length in meters.

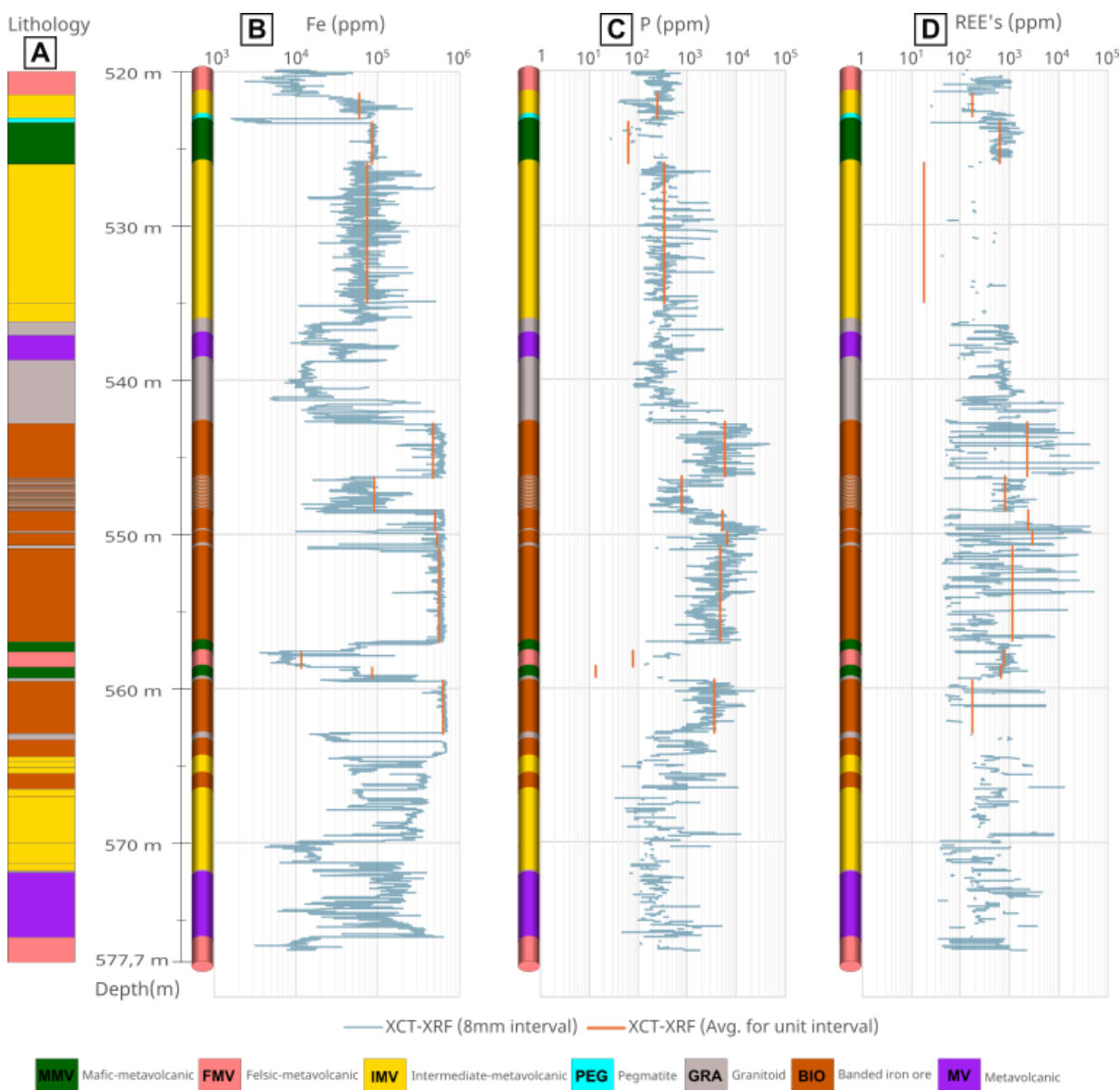


Figure 11 A-D. XCT-XRF scan results, 8 mm and unit intervals (from Table 1), and lithological core log for drill hole BB-14-013.

- (A) Simplified core log showing lithological units.
- (B) Downhole plot of the distribution of Fe (ppm) based on XCT-XRF concentration data
- (C) Downhole plot of the distribution of P (ppm) based on XCT-XRF concentration data
- (D) Downhole plot of the distribution of total REE (ppm) based on XCT-XRF concentration data.

Phosphorus concentrations follow Fe systematically and display localized enrichment in specific BIO intervals (Fig. 11C). Unit 7 (549.9-550.7 m) contains the highest P value at 0.66 wt.%, followed by Unit 4 (542.8-546.3 m) and Unit 6 (548.5-549.8 m), with concentrations of 0.57 wt.% and 0.52 wt.%, respectively. All these units are logged as BIO and described in the core log as containing varying proportions of hematite and magnetite, often with fine foliation or banding. The metavolcanic units consistently display P levels beneath the selected limit of 0.1 wt.%, indicating an absence of significant mineral phases.

The REE's clearly follow the same trend as P concentrations, with their highest enrichment within some BIO intervals. Similarly to that described above for P, unit 7 shows the highest REE content at 2915 ppm, followed by Unit 4 (2316 ppm) and Unit 6 (2322 ppm). Unit 8 (1135 ppm) exhibits a concentration just above the selected lower limit, its notably greater length (6.05 m), however, includes localized intervals of elevated REE values corresponding to those observed in Units 4, 6 and 7, indicated by the peaks in Figure 11D. In all the metavolcanic units the concentrations fall below 0.1 wt. %.

In summary the elemental concentration profiles from the XCT-XRF scanning for Fe, P and REE's closely reflect the lithological variation logged in the core. BIO units consistently exhibit correlating elevated values of these elements, whereas metavolcanic units lack significant concentration of the same. These patterns define the BIO units as the primary zones of interest within the studied drill core, with emphasis on Units 4, 6, 7.

5.4 Host minerals for REEs

5.4.1 Analysis from Insight

Two examples of representative sections from the main ore body in drill core BB-14-013, obtained from 3D tomographic imaging (XCT) using Orexplore Insight software, are shown in Figure 12. Light, or colourless, areas indicating minerals like quartz or apatite with attenuation values below 2. Red areas represent the iron oxides hematite and magnetite with attenuation values at around 4. Bright yellow patches represent the highest attenuating minerals like monazite, xenotime and allanite. The yellow colouring on the edges of the cut surface is an analytical artefact and doesn't relate to the mineralogy.

The first section (Fig. 12A) illustrates the characteristic structure of the ore body, consisting of alternating bands of iron oxides and light-coloured layers. The corresponding concentration profiles of REE's and phosphorus, aligned with the 3D XCT-XRF image, indicate an enrichment of REE-bearing phases within the light-coloured band near the centre of the scanned interval. Among the detected REE's, cerium exhibits the highest concentration, reaching up to 26000 ppm (averaged at 8mm intervals), alongside a phosphorus concentration of 48000 ppm. This geochemical signature suggests the potential presence of monazite (CePO_4). Lanthanum and neodymium display lower concentrations in the same zone (7200 ppm and 6800 ppm, respectively), consistent with partial substitution in the monazite structure. Yttrium reaches concentrations of up to 2100 ppm, which may indicate the presence of xenotime (YPO_4) although it appears to be less abundant than monazite.

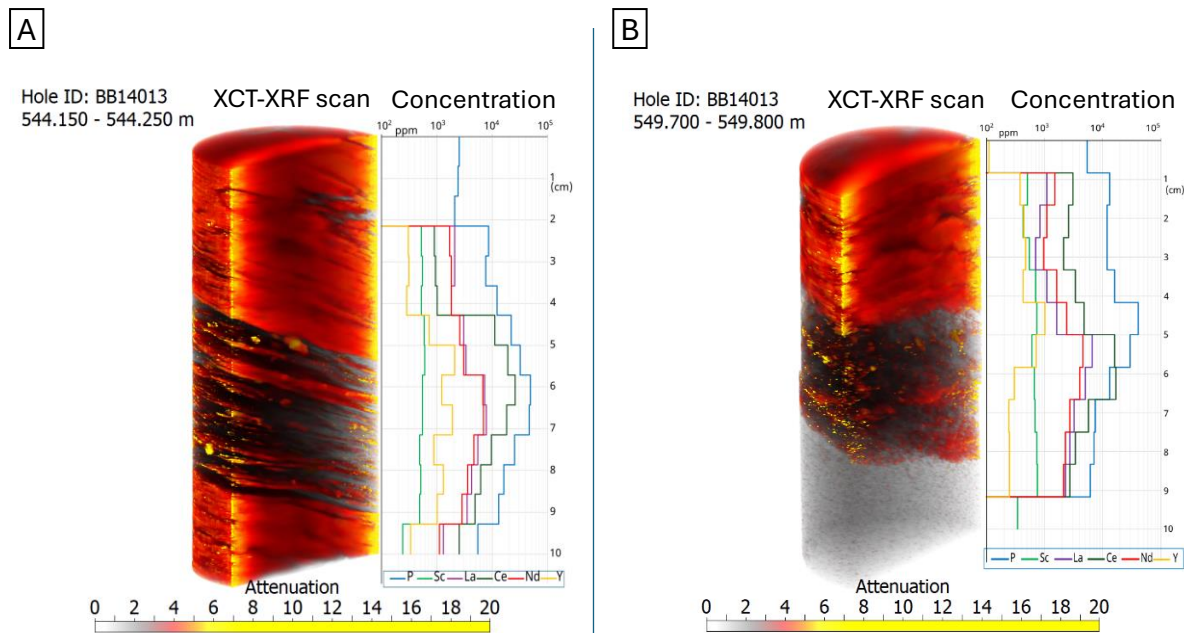


Figure 12 A-B. Two examples of representative sections from the main ore body in drill core BB-14-013, obtained from 3D tomographic imaging (XCT-XRF) with corresponding concentration profiles of REE's and phosphorus, from Orexplore Insight software. Colours in the drill core image represent phases with attenuation values, based on attenuation scale at the bottom of images.

(A) 10cm section between 544.15 m - 544.25 m.

(B) 10cm section between 549.7 m – 549.8 m.

The second section (Fig. 12B) illustrates a section of the drill core where the main ore body has been crosscut by a granitic vein. Enrichment of REE's and phosphorus is observed along what appears to be an altered contact zone between the iron oxides and the granite. The 3D XCT-XRF image reveals scattered, high-attenuation phases in the upper iron oxide portion, which become increasingly abundant within the contact margin. These zones correspond with elevated concentrations of P and REE's. Toward the lower part of the interval, where the granitic intrusion dominates, concentrations of these elements drop sharply. This geochemical and structural signature suggests that REE-bearing phases extend beyond the main ore body, particularly into zones where contact-related alteration has occurred. Below 6 cm in the section from Fig. 12B, cerium concentrations exceed phosphorus (17000 ppm and 13000 ppm respectively), which may indicate the presence of a non-phosphorus REE-bearing mineral, like allanite $((Ca,Ce,La,Y)_2(Al,Fe^{3+})_3(SiO_4)_3(OH))$.

Table 2. SEM-EDS analyzed mineralogy in samples from drill core BB-14-013 from Blötberget

Sample	Depth (m)	Lithology	Description	FAp	Mnz	Xtm	Aln	REE-Fcarb	Hem	Mt
B-13-544B	544.0	BIO	Hem-dominant	+		+	+	+	+	
B-13-544.2A	544.2	BIO	Hem-dominant	+	+	+		+	+	
B-13-546A	546.0	BIO	50/50 Hem+Mt	+	+		+	+	+	
B-13-549.5B	549.5	BIO	Hem-dominant	+	+	+			+	+
B-13-549.7	549.7	BIO w. GRA vein	Hem-dominant	+	+		+		+	
B-13-550.2	550.2	BIO	Hem-dominant	+	+	+			+	
B-13-560.2	560.2	BIO	Hem-dominant	+	+	+	+	+	+	+

Notes: FAp=Fluorapatite, Mnz=Monazite, Xtm=Xenotime, REE-Fcarb=REE-bearing fluorcarbonate, Hem=hematite, Mt=Magnetite

5.4.2 Analysis from SEM-EDS

In this study, all seven samples selected from the main ore body of the drill core and analysed by SEM-EDS were found to contain both fluorapatite and REE-bearing phases (Table 2). The identified REE-bearing phases include monazite-(Ce), xenotime-(Y), allanite-(Ce) and a REE-bearing fluorcarbonate. It should be noted that EDS analyses are generally regarded as semi-quantitative.

Fluorapatite occurs predominantly in two distinct textural types (Table 3). The first consists of euhedral grains lacking inclusions (Fig. 13a), while the second comprises larger, anhedral grains that host numerous inclusions (Fig. 13b). These inclusions are primarily monazite, although xenotime and allanite are also present. They tend to be concentrated toward the cores of the fluorapatite grains, with fewer inclusions observed at the rims (Fig. 13b).

According to SEM-EDS analysis performed in this study elemental compositions of the two textural types do not differ significantly. It should be noted that oxygen concentrations are inferred based on mineral stoichiometry and were not directly measured. No fluorapatite grain in this study exhibited detectable concentrations of REE's under SEM-EDS analysis.

Table 3. Representative fluorapatite (wt%)

Sample	type	O	F	P	Ca	Sum elements	P2O5	CaO	Sum oxides
B-13-544.2A	euohedral grain	38,05	3,87	17,58	38,44	97,93	40,29	53,78	94,07
B-13-544.2A	euohedral grain	37,91	3,19	17,58	38,1	96,79	40,28	53,31	93,6
B-13-544.2A	euohedral grain	39,36	4,23	18,27	39,51	101,37	41,86	55,29	97,15
B-13-544.2A	euohedral grain	35,79	3,57	16,59	36	91,95	38,01	50,37	88,38
B-13-544B	euohedral grain	38,25	4,19	17,77	38,34	98,55	40,72	53,64	94,35
B-13-544B	euohedral grain	41,78	4,53	19,32	42,16	107,79	44,27	58,99	103,26
B-13-546A	euohedral grain	38,7	3,94	17,88	39,09	99,61	40,97	54,7	95,67
B-13-546A	euohedral grain	39,24	3,87	18,18	39,49	100,78	41,66	55,25	96,91
B-13-546A	euohedral grain	38,79	4,06	17,96	39,07	99,89	41,16	54,67	95,83
B-13-549.5B	large grain w. inclusions	39,06	3,72	18,09	39,31	100,18	41,46	55	96,46
B-13-549.5B	euohedral grain	38,88	3,9	18,05	38,91	99,74	41,36	54,45	95,95
B-13-549.5B	euohedral grain	41,08	4,07	19,04	41,31	105,5	43,63	57,8	101,43
B-13-549.7	euohedral grain	38,53	4,29	17,87	38,73	99,42	40,94	54,19	95,13
B-13-549.7	euohedral grain	35,09	3,65	16,19	35,54	90,47	37,1	49,72	86,82
B-13-550.2	large grain w. inclusions	37,67	3,73	17,44	37,95	96,79	39,96	53,1	96,79
B-13-550.2	large grain w. inclusions	39,12	4,12	18,16	39,26	100,66	41,6	54,93	100,66
B-13-550.2	euohedral grain	41,6	4,28	19,29	41,81	106,98	44,21	58,49	106,98

Notes: Oxygen concentrations are inferred based on mineral stoichiometry, not measured

Monazite-(Ce) exhibits several different textural types across the analysed samples (Table 4). However, a general classification can be made to group them into two primary textures. The first consists of discrete monazite grains, commonly located adjacent to fluorapatite (Fig. 13c), while the second comprises monazite inclusions hosted within the larger fluorapatite grains (Fig. 13d). According to SEM-EDS analysis, the mean composition of the two monazite types differs only slightly.

Table 4. Representative monazite compositions (wt%)

Sample	type	SiO ₂	P ₂ O ₅	SO ₃	CaO	Y ₂ O ₃	Fe ₂ O ₃	La ₂ O ₃	Ce ₂ O ₃	Pr ₂ O ₃	Nd ₂ O ₃	Sm ₂ O ₃	Gd ₂ O ₃	ThO ₂	Sum
B-13-544.2A	grain next to hem	28,50	0,70	0,54			0,84	16,07	33,09	3,38	12,22	1,84	1,08		98,25
B-13-544.2A	grain next to hem+FAp	27,80						14,07	29,99	3,11	13,92	2,32	1,32		92,55
B-13-544.2A	grain next to hem+FAp	0,37	28,87	0,54	0,35	1,35		14,78	31,72	3,13	12,74	1,87	1,27		97,25
B-13-544.2A	grain next to hem+FAp	0,48	28,18	0,74	0,48			15,55	32,63	3,22	12,01	1,48	0,92		95,70
B-13-544.2A	grain edge FAp	26,77			0,58			9,63	27,94	3,80	16,73	2,79	1,69		89,93
B-13-544.2A	grain next to hem+FAp	0,33	28,65	0,82	0,46	0,92		14,44	33,17	3,42	13,78	2,00	0,87		98,87
B-13-549.5B	inclusion large FAp	24,30			0,38			11,98	27,03	2,61	11,21	1,73	1,04	0,79	81,07
B-13-549.5B	inclusion large FAp	0,31	24,23	0,47	0,44	1,30		11,94	27,20	3,00	11,17	1,64	1,16		83,19
B-13-549.5B	grain next to hem	0,46	26,77		0,26			13,78	30,02	3,14	12,49	1,75	1,37		90,58
B-13-549.5B	grain next to hem+FAp	0,25	27,69	0,38	0,39	1,44		13,02	30,88	3,72	13,65	2,06	1,38	0,80	95,65
B-13-549.5B	grain next to hem+FAp	29,21		0,43	0,39	1,76		13,90	32,13	3,31	13,36	2,03	1,26		98,16
B-13-549.7	inclusion allanite	29,22			0,44			20,11	31,86	2,71	10,62	1,22			96,18
B-13-549.7	large grain next to FAp	0,54	24,37	0,68	0,46			16,51	28,70	2,66	9,14	0,92			83,98
B-13-549.7	large grain next to FAp	0,44	24,97	0,53	0,41			16,64	29,12	2,17	9,34				83,62
B-13-550.2	Inclusion big FAp	24,97			0,50			12,65	28,17	3,32	11,50	1,72	1,21		83,90
B-13-550.2	Inclusion big FAp	27,03		0,64	0,41	1,81		12,82	30,23	3,11	12,45	1,97	1,13		91,59
B-13-550.2	larger grain next to FAp	29,93			0,44	1,94		14,61	32,02	3,20	13,57	2,26	1,54	0,68	100,18
B-13-560.2	larger grain	0,74	26,00	0,85	0,51			17,42	30,88	2,58	9,61				89,09
B-13-560.2	medium sized grain	0,58	29,49		0,70		0,62	14,31	31,09	3,40	14,77	2,49	1,56	1,07	100,07
B-13-560.2	inclusion big FAp	0,66	28,31	0,75	0,51			18,70	32,55	2,65	10,44	1,15		0,86	96,57
B-13-560.2	larger grain	0,63	27,60	0,72	0,40			17,07	32,85	2,69	11,22				93,17

Notes: blank= measured for but not detected. Oxygen concentrations are inferred based on mineral stoichiometry, not measured

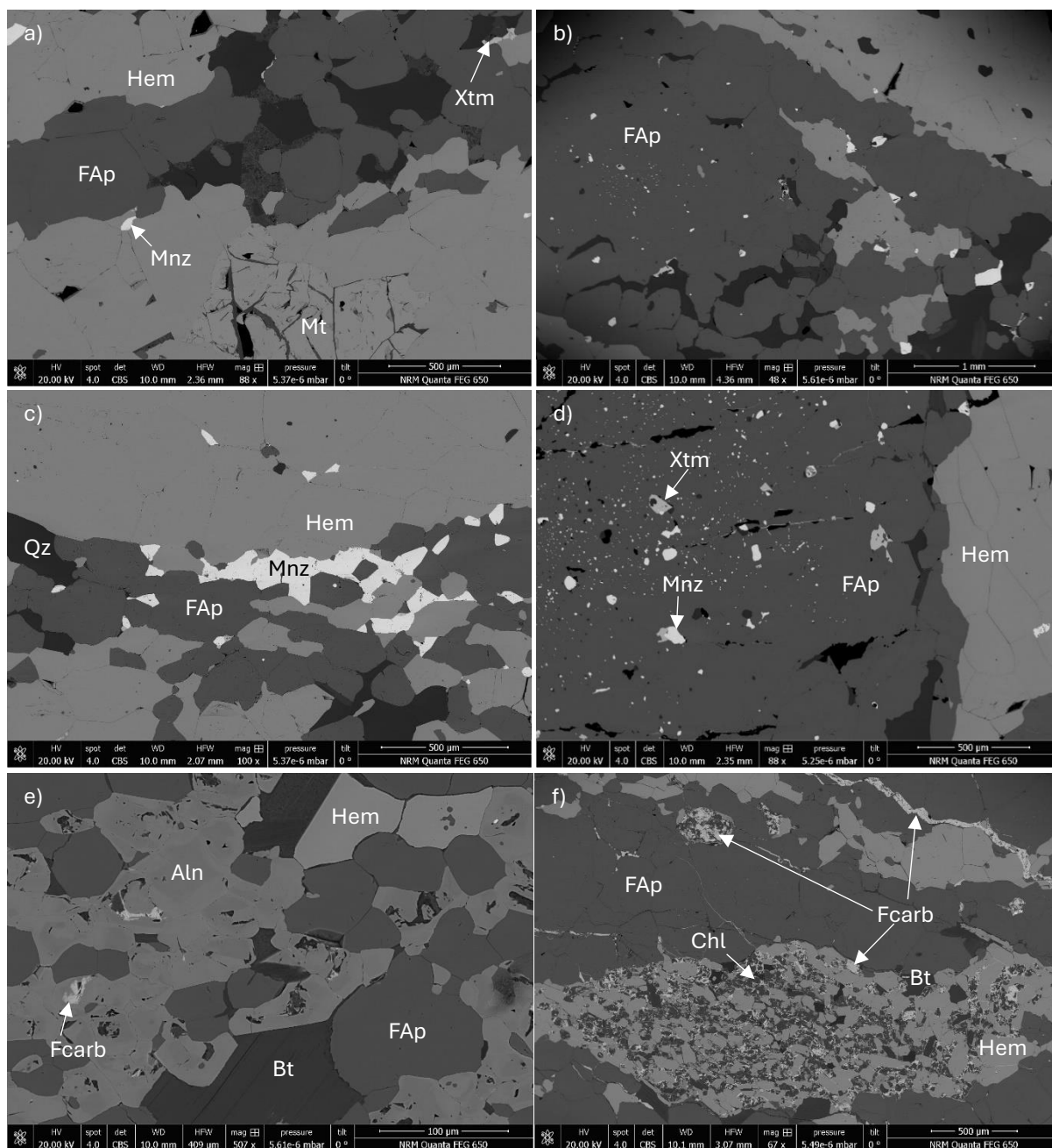


Figure 13 a-f. SEM-EDS images of host minerals for REEs

- a)** Sample B-13-549.5B showing euhedral FAp grains, accompanied by hematite, magnetite, monazite and xenotime.
- b)** Sample B-13-550.2 showing a larger anhedral FAp grain with numerous inclusions.
- c)** Sample B-13-544.2A showing individual grains of monazite, with neighbouring fluorapatite and hematite grains
- d)** Sample B-13-550.2 showing a larger anhedral FAp grain with numerous inclusions. Inclusions are dominantly monazite, however xenotime is also present. Hematite is the accompanying iron oxide.
- e)** Sample B-13-546A showing subhedral to euhedral zoned allanite grains. The cores display a slightly darker grey compared to the rims. Also present is hematite, biotite, fluorapatite and interstitial fluorcarbonate.
- f)** Sample B-13-544B showing REE-bearing fluorcarbonate phase. It appears in fractures as well as altered infill material occupying interstitial spaces between hematite, biotite, chlorite and fluorapatite grains

Table 5. Representative xenotime compositions (wt%)

Sample	type	SiO ₂	P ₂ O ₅	CaO	As ₂ O ₃	Fe ₂ O ₃	Y ₂ O ₃	Nd ₂ O ₃	Sm ₂ O ₃	Gd ₂ O ₃	Dy ₂ O ₃	Ho ₂ O ₃	Er ₂ O ₃	Tm ₂ O ₃	Yb ₂ O ₃	Lu ₂ O ₃	IrO ₂	Sum
B-13-544.2A	small grain next to FAp	31,35	0,40	0,64		40,78				2,23	4,81	0,93	4,10		3,31			88,54
B-13-544.2A	small grain next to FAp	32,22				1,05	41,78	0,37	0,41	2,18	4,90	1,37	4,18	0,72	3,71			92,90
B-13-544B	inclusion in hem	32,49				2,20	42,73			1,90	4,76	1,00	3,91		3,67			92,66
B-13-549.5B	inclusion big FAp	0,56	33,89	0,14			46,60	0,40	0,62	2,14	4,83	1,12	4,91	0,75	4,36		0,14	100,44
B-13-549.5B	edge of hem+FAp		33,00				42,69		0,64	2,42	4,99	1,23	3,96		3,69			92,61
B-13-549.5B	small grain next to FAp		30,65				40,20	0,34	0,43	2,23	5,05	1,32	4,01	0,57	3,15			87,96
B-13-550.2	inclusion big FAp		30,23	0,14			39,26	0,38	0,45	1,95	4,30	1,07	4,22	0,81	4,47			87,27
B-13-550.2	inclusion big FAp		32,52				41,98		0,45	2,56	4,99	1,22	4,41		4,21			92,57
B-13-550.2	inclusion big FAp		35,18				45,71		0,56	2,13	4,82	1,29	4,79		4,78	0,74		100,02
B-13-560.2	inclusion big FAp	0,68	34,22		0,83		45,58	0,41	0,68	1,88	4,42	1,36	4,75	0,78	4,71	0,67		100,98

Notes: blank= measured for but not detected. Oxygen concentrations are inferred based on mineral stoichiometry, not measured

Texturally, xenotime closely resembles monazite. It occurs both as inclusions within the larger fluorapatite grains (Fig. 13d) and as discrete grains (Table 5). However, xenotime differs from monazite in both abundance and grain size, generally being less common and smaller. When present outside of fluorapatite, xenotime typically occurs either as very small discrete grains or as interstitial phases between iron oxides and fluorapatite (Fig. 13a).

Allanite-(Ce) was identified in four samples (Table 6), typically occurring as euhedral to subhedral grains that exhibit zoning. In two of the samples (B-13-546A and B-13-549.7) they appear abundantly, both of these samples are obtained from the main ore body within contact zones close to granitic veins. Under SEM-EDS analysis, the rims of zoned grains commonly display a slightly lighter grey tone compared to their cores (Fig. 13e), suggesting enrichment in REEs towards the grain margins. Allanite is frequently observed in close association with biotite, often accompanied by radiation halos burned into the biotite grains. The presence of these radiation halos supports the presence of radioactive elements (e.g. Th and/or U) within the allanite structure. However, their absence in the measured spectra may reflect detection limits of the instrument rather than their actual absence. Notably, all measured allanite contains minor amounts of MgO.

Table 6. Representative allanite compositions (wt%)

Sample	Type	MgO	Al ₂ O ₃	SiO ₂	CaO	Fe ₂ O ₃	Y ₂ O ₃	La ₂ O ₃	Ce ₂ O ₃	Pr ₂ O ₃	Nd ₂ O ₃	Sm ₂ O ₃	Sum
B-13-544B	euhedral grain	1,28	15,71	29,81	11,60	13,55		5,49	10,62	1,18	3,65	0,63	93,51
B-13-546A	euhedral grain	1,67	16,51	30,65	12,89	12,91		5,14	9,54	0,99	3,53		93,82
B-13-546A	euhedral grain	1,55	17,37	31,89	14,36	13,21	0,45	4,45	8,56	0,78	2,95		95,58
B-13-546A	inclusion FAp	1,31	17,16	30,68	14,50	12,72		3,65	7,04	0,85	3,11	0,53	91,57
B-13-546A	euhedral grain	1,68	16,69	30,81	12,97	13,17		5,01	9,71	0,81	3,56		94,41
B-13-546A	euhedral grain	1,57	16,99	31,46	12,74	13,51		5,35	9,98	0,98	4,06	0,59	97,21
B-13-546A	euhedral grain	1,64	16,81	31,12	13,60	13,47		4,52	8,77	0,85	3,34	0,58	94,69
B-13-549.7	euhedral grain	1,54	15,81	29,10	12,49	12,47		5,10	8,50	0,91	2,59	0,48	88,98
B-13-549.7	euhedral grain	1,68	14,94	28,85	11,67	12,95		6,00	10,15		2,58		88,83
B-13-549.7	euhedral grain	1,89	16,79	32,39	13,19	14,42		6,50	11,06	0,86	3,01		100,11
B-13-549.7	euhedral grain	1,29	17,08	30,94	12,96	13,49		5,40	9,74	1,05	3,18	0,55	95,68
B-13-549.7	euhedral grain	0,84	15,04	26,57	11,01	11,30		4,71	8,35	0,78	2,72		81,32
B-13-560.2	altered grain	1,46	15,45	29,92	10,81	13,91		5,32	11,35	1,27	4,73	0,70	94,92

Notes: blank= measured for but not detected. Oxygen concentrations are inferred based on mineral stoichiometry, not measured

The REE-bearing fluorcarbonate phase identified in the samples typically contains substantial concentrations of the light REEs. However, interpretation of these phases is constrained by the lack of carbon detection in the SEM-EDS analysis, preventing definite confirmation on the values. Nonetheless, their presence is noteworthy. Texturally they occur as altered infill material occupying interstitial spaces between hematite, monazite, allanite, biotite, chlorite and fluorapatite grains, as well as within fractures (Fig. 13f).

5.5 Comparison between XCT-XRF and assay data

To evaluate the reliability of the XCT-XRF scanning method, geochemical assay data provided by Nordic Iron Ore from the same drill core were used for comparison. This data was produced at ALS commercial laboratories.

Six key elements and oxides provided in the assay data are also available in the XCT-XRF data: SiO₂, Fe, CaO, P, TiO₂, and total REEs (Fig. 14). Each plot displays a number of datapoints, a 1:1 reference line, a regression trendline and the calculated R² value to evaluate the correlation between XCT-XRF scanning and assay data. Datapoints above the 1:1 line indicate that the scanning method overestimated the concentration relative to assay data, while points below the line indicate underestimation. The datapoints represent the intervals in the core that were taken for assay and the XCT-XRF data was extracted from the Insight software for exactly the same intervals to allow direct comparison. The major elements SiO₂, Fe, CaO, P and TiO₂ were assayed in different intervals from 524.93 m to 576.07 m depth. The REEs were only assayed in the main ore body, between 542.71 m to 569.86 m.

For major elements such as SiO₂, CaO and Fe the XCT-XRF results show strong linear correlation with assay values, with R² values ranging from 0.97 to 0.99, as well as plotting close to the 1:1 line (Fig. 14). While for TiO₂ and P, despite exhibiting a close linear correlation, the scanning method overrepresents and underrepresents respectively relative to assay concentrations. In contrast, the correlation for total REEs is notably weaker (R² = 0.63) indicating higher variability, together with a general trend where the scanning method underrepresents concentrations compared to assay (Fig. 14).

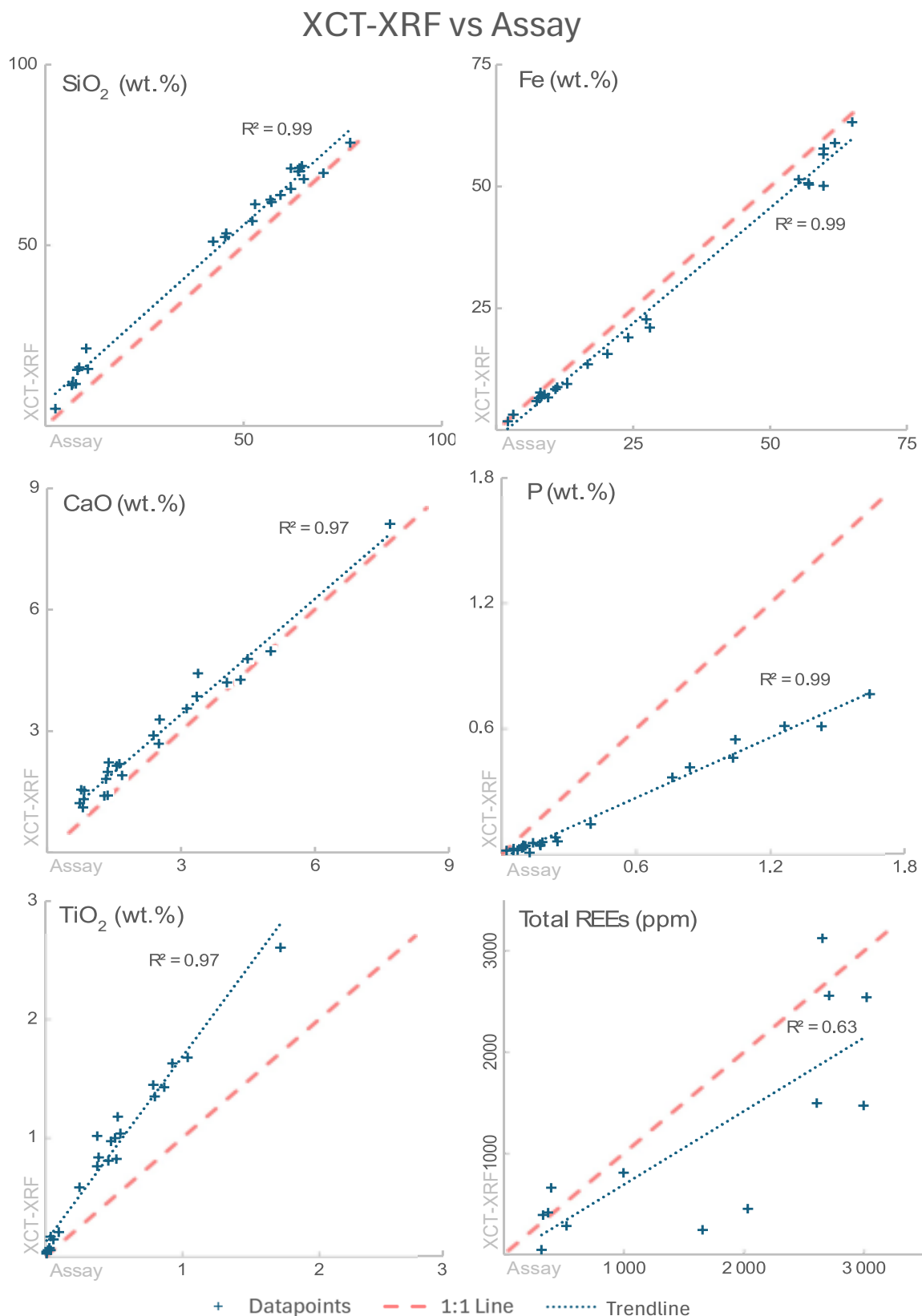


Figure 14. Comparison of elemental and oxide concentrations obtained from XCT-XRF scanning (y-axis) and geochemical assay data (x-axis) for six selected variables in the drill core. The plots include both major oxides (SiO₂, CaO, TiO₂) and elemental forms (Fe, P, Total REEs). Each plot shows a 1:1 reference line (red, dashed), a linear regression trendline (blue, dotted) and the calculated coefficient of determination (R^2). Concentrations are reported in weight percent (wt.%) for SiO₂, CaO, TiO₂, Fe and P, while total REE's are expressed in parts per million (ppm).

6. Discussion

One of the primary aims for this study was to assess the effectiveness of XCT-XRF scanning in detecting and characterizing REE-bearing minerals within the Blötberget drill core BB-14-013. The results obtained from this non-destructive technique were compared to assay data as well as assisted by conventional analytical methods (optical petrography and SEM-EDS).

6.1 Evaluation of XCT-XRF performance

To evaluate the reliability of the XCT-XRF scanning method for this type of deposit, concentrations from scanning were compared with conventional assay data. The comparison (Fig. 14) shows a very strong linear correlation for SiO₂, Fe, CaO, P and TiO₂ with R² values ranging from 0.9682 to 0.9915. However, total REEs exhibit a notably weaker correlation (R² = 0.6291), suggesting greater variability and limited predictability for these elements.

In cases like TiO₂, the scanning consistently overestimates concentrations compared to the assay. This likely reflects a beam hardening effect, where the Fe-rich matrix causes selective attenuation of low-energy X-rays, which artificially overrepresents higher-energy signals like those from heavier elements (e.g. Ti) (Kyle & Ketcham, 2015). Conversely, lighter elements such as P, which emit lower-energy X-rays, appear to be systematically underrepresented by the scanner. These matrix-related effects are well documented in CT-based systems (Kyle & Ketcham, 2015), as there are always density contrasts in rocks, but are particularly pronounced here due to the high-density, Fe-rich nature of the Blötberget ore. Although the strong correlations for major elements indicate that XCT-XRF scanning reliably captures overall geochemical trends, the deviation from the 1:1 line emphasizes that absolute concentrations should be interpreted cautiously, especially where high density matrix effects may be significant.

The down-hole REE signal from the XCT-XRF data displays a distinctly “spiked” pattern with sharp peaks and flat troughs in REE-concentrations (Fig. 11d and 12). This pattern may not reflect the true REE distribution throughout the core. The XRF scans the outer few millimetres of the surface of the core and the peaks may well be areas where we see the high attenuation REE phosphates. While, the spikes likely correspond to locations where REE-bearing phosphate minerals, such as monazite or xenotime, occur at or near the surface of the scanned core section, where their dense and X-ray attenuating nature allows them to be clearly detected by the scanner. The troughs, however, often register values close to zero, which likely reflects instances where REEs are present but below detection limit of the scanner. In such zones, REEs may still be present but not in concentrations or positions detectable by surfaced-based XRF. For example, they could occur in phases like fluorapatite where they have lower concentrations, or within monazite or xenotime which is located in the centre of the drill core rather than the surface. This produces an REE pattern: the peaks are real, indicating areas of elevated REE concentrations, but the absence of signal in the troughs is not necessarily indicative of true lack of REEs. Instead, it highlights the spatial and mineral-specific limitations of the method, where only near-surface, REE-rich mineral phases are registered.

Therefore, while XCT-XRF scanning can detect REE enrichment zones, it most likely does not capture their full distribution throughout the core under the settings used for this study. The scanning method should be seen as a semi-quantitative tool that effectively identifies enrichment but lacks the sensitivity for detecting diffuse or low-grade REE-bearing phases.

The XCT-XRF scanning successfully highlighted some REE-enriched zones, particularly where monazite, xenotime and allanite were present as discrete or inclusion-bearing grains.

These areas correspond well with elevated concentrations of Ce, La, Nd and Y in the scanning data. For example, sample B-13-544.2A, collected from the BIO unit 4 (Table 1) showing REE and P enrichment in XCT-XRF data (Table 1 and Fig. 12A), aligns with zones where petrography (Fig. 8) and SEM-EDS (Fig. 13c) confirmed the presence of monazite as discrete grains. Uncertainties, however, remain as to whether other zones of interest might exist in the drill core, since data from the scanner have been shown to generally underestimate REE concentrations compared to conventional assays (Fig. 14), as well as the limited extent of comparable assay data.

6.2 REE distribution patterns

The spatial distribution of REEs in the Blötberget drill core, as observed from XCT-XRF data and supported by petrography and SEM-EDS, shows that REEs are largely confined to the banded iron ore (BIO) sequence. No significant enrichment was identified in the surrounding lithologies, suggesting that REEs are spatially associated with the main ore body.

Within the main ore body, REE concentrations vary between units. Notably, Unit 7 exhibits the highest average total REE content at 2915 ppm, followed by Unit 6 (2322 ppm) and Unit 4 (2316 ppm) (Table 1). These units also correspond to zones of elevated phosphorus, supporting the interpretation that REEs are hosted primarily in phosphate minerals. This gives support for the use of phosphorus as a general proxy for REE distribution, although exceptions exist. In some instances, enrichment appears locally concentrated along lithological contact zones adjacent to granitic intrusions, indicating that localized REE enrichment occurs within the ore body. Notably, abundant allanite was found in two samples near the contact margins of granitic veins perhaps suggesting recrystallisation of the primary phosphates to silicate minerals during late-stage intrusion of the granite.

While both hematite- and magnetite-dominated sections occur in the drill core, this study found no systematic difference in REE abundance between the two. In most samples examined, hematite appeared to be the dominant iron oxide associated with REE phases. However, the limited number of thin sections, all largely hematite-dominant, may obscure any subtle trends.

These findings indicate that REEs are predominantly contained within the ore zones already targeted for iron extraction. This implies that REE-bearing minerals are likely to be mined as part of the Fe-ore operations, reducing the need to process additional host rock.

6.3 Host minerals for REEs

This study identified the primary REE host phases at Blötberget to be the phosphate minerals monazite-(Ce) and xenotime-(Y), typically occurring as discrete grains or as inclusions within fluorapatite. Monazite typically enriched in the light rare-earth elements (LREE) and xenotime in heavy rare-earth elements (HREE). These REE-bearing phases are most frequently associated with the iron oxide-rich layers in the main ore body, particularly in proximity to fluorapatite, suggesting a strong paragenetic relationship.

No detectable REEs were found in fluorapatite itself via SEM-EDS; however, this may reflect the instruments limitations rather than true absence. A study on the same SEM system (at the Museum of Natural History, Stockholm) using the 'Durango apatite' reference material and 40 second count time reported Ce_2O_3 concentrations of 0.5 ± 0.23 wt.% which is suggested being close to the detection limit for the instrument (Andreas Karlsson, pers comm). This implies that low REE contents may simply fall below the instrument's sensitivity. This is also confirmed by recent results in a currently ongoing research project at

Gothenburg University which report Ce_2O_3 concentration in apatite from Blötberget at < 0.1 wt.% (Leopold Chicoine, pers comm). This contrasts with Jonsson et al. (2016), who found significant REEs (mean compositions between 0.19 – 1.73 wt.% total $(\text{Y}+\text{REE})_2\text{O}_3$) in fluorapatite from the nearby Grängesberg deposit using EMP (Electron Microprobe) analysis. Given the volumetric abundance of fluorapatite in the ore at Blötberget, even low REE concentrations could make it a major contributor to the total REE budget, potentially surpassing the less abundant phases monazite and xenotime, despite their higher individual REE concentrations.

Allanite-(Ce), enriched in LREE, was mainly observed in two samples near the margins of granitic veins. This spatial association suggests the possibility of localized remobilization or recrystallization of REE-bearing phases via magmatic or hydrothermal processes related to granitic intrusions. Though based on limited data, the occurrence of allanite supports the idea that silicate-hosted REEs may form in response to late-stage alteration.

These findings align with previous work by Jiao (2011), who also studied the Blötberget deposit. While Jiao's study largely focused on characterizing and investigating the genesis of the IOA ores and their host rocks at Blötberget, similar observations are made about REE-bearing phases with this study. Both studies report that major REE carriers are predominantly monazite, xenotime and allanite, and that these minerals are typically found in close association with fluorapatite within the iron oxide-rich zones.

Together, these observations point to a mineralogically diverse REE assemblage, with phosphate minerals dominating, but silicate-hosted phases like allanite occurs, particularly near intrusive contacts within the main ore body. From a processing standpoint, this suggests

that P may serve as a useful proxy for identifying REE-rich zones, however, its effectiveness is limited in areas where allanite dominates as the primary REE host.

6.4 Implications

In terms of methodology, the use of XCT-XRF in this study highlights the potential of integrating non-destructive scanning into early-stage exploration work. XCT-XRF proved to a certain degree valuable for identifying REE-enriched zones on a broad scale, offering a spatial extensive overview of a drill core. However, the technique's limitations, such as detection thresholds and interference from dense iron oxides, mean that XCT-XRF data must be carefully ground-truthed with petrographic and microanalytical methods like SEM-EDS. Together, these tools provide a complementary dataset that improves confidence.

The result of this study has implications for both the understanding of REE distribution within the Blötberget deposit and for potential extraction strategies. The REEs are not evenly distributed throughout the drill core but are instead concentrated in specific lithological and textural settings. They occur predominantly in phosphate minerals such as monazite and xenotime, which are frequently associated with fluorapatite rich zones within the banded iron ore. However, some contact margins at granitic intrusions in the banded iron ore have also been shown to contain enrichment in REEs in the form of silicate minerals like allanite.

From an economic perspective, the lithology-specific distribution of REEs has important implications for mining and extraction strategies. This study demonstrates that REEs are primarily confined to the main ore body, and that phosphorus can generally serve as a proxy for REE enrichment. Since REEs are largely restricted to the iron ore, it implies that bulk extraction of the ore is likely to recover most of the REE content, regardless of whether

additional process steps, such as separation by floatation, are required. While detailed metallurgical mining analysis is outside the scope of this paper, the observed mineralogy suggests that specific processing techniques for efficient REE recovery may be required, as has been discussed for similar REE deposits (e.g., Haque et al., 2014; Jordens et al., 2013).

6.5 Suggestions for further research

A more comprehensive understanding of REE distribution and recoverability at Blötberget will require additional research in the following areas:

- Broader sampling:

More sample analysis across different lithologies and structural zones are needed to fully determine whether REE-bearing minerals are widespread or spatially restricted.

- Expanded assay coverage:

Additional REE assay data would improve the reliability of comparisons with XCT-XRF results and clarify the true extent of REE enrichment throughout the deposit

- Quantitative microanalysis:

High-resolution techniques, such as EMP or LA-ICP-MS, could be applied to accurately quantify REE contents in individual minerals, assess detection limits and evaluate how much REE may be hosted in phases like apatite, that may not be fully captured by SEM-EDS.

These steps would strengthen the overall understanding of REE distribution and help determine whether targeted exploration and processing strategies are necessary.

7. Conclusions

- ◆ The XCT-XRF scanner successfully detected REE-enriched zones associated with high-density phases but tended to overestimate some elements (e.g. Ti) and underestimate others (e.g. P and REEs) compared to conventional assay data, likely due to beam hardening effects from the Fe-rich matrix and detection limits.
- ◆ REEs were found to be spatially confined to the banded iron ore units, with the highest concentrations aligning with phosphorus-rich zones, supporting the general use of P as a proxy. However, exceptions such as silicate-hosted REEs near granitic veins highlight deviations from this trend.
- ◆ The primary host minerals for REEs were identified as monazite-(Ce) and xenotime-(Y), typically occurring in or near fluorapatite. Allanite-(Ce) was also identified, particularly near granitic vein margins, possibly linked to late-stage remobilisation processes.
- ◆ No REEs were detected in fluorapatite via SEM-EDS; however, the limitations of the method suggest that low-level REE concentrations may still be present, emphasizing the need for more sensitive analytical techniques.
- ◆ From a mining perspective, the confinement of REEs within the ore body suggests that they can be recovered during conventional iron ore extraction, although additional processing will be required to separate REE-bearing minerals such as monazite, xenotime and allanite
- ◆ The initial hypothesis - that the combined XCT-XRF scanning together with geochemical and mineralogical analysis could reliably detect and characterize REE-bearing minerals – was partially supported. The methods effectiveness lies in the combined effort where each step served its important role.
- ◆ In a broader context, by contributing new insights into REE distribution at Blötberget, this study supports the goal of strengthening domestic REE exploration, a crucial step towards European independence and a more secure, sustainable supply chain of critical raw materials.

8. Acknowledgements

First and foremost, I would like to express my deep gratitude to Iain Pitcairn at Stockholm University for his invaluable supervision throughout this project. His guidance, from the initial stages of setting up the study to the final interpretations, has been essential to the outcome of this thesis. I am also sincerely thankful to Andreas Karlsson at the Museum of Natural History, Stockholm, for his support and expertise during the SEM-EDS analyses, and for insightful input on the resulting data. I would like to thank Alexander Hansson at Orexplore for his assistance in using the GeoCore X10 and for contributing valuable interpretations during the data evaluation phase. A special thanks to Maria Arnover, a fellow student working on a similar topic, for the enjoyable collaboration and shared motivation during many of the practical aspects of the project. I also appreciate Laurens Tromp for his help with carbon coating the samples for SEM-EDS analysis, and Leopold Chicoine for providing spot analyses of apatite using LA-ICP-MS.

Finally, I am deeply grateful to my family for their unwavering love, support and encouragement throughout the entire process.

9. References

- Allen, R. L., Lundstrom, I., Ripa, M., & Christofferson, H. (1996). Facies analysis of a 1.9 Ga, continental margin, back-arc, felsic caldera province with diverse Zn-Pb-Ag-(Cu-Au) sulfide and Fe oxide deposits, Bergslagen region, Sweden. *Economic Geology*, *91*(6), 979–1008. <https://doi.org/10.2113/gsecongeo.91.6.979>
- Almqvist, B. S. G., Björk, A., Mattsson, H. B., Hedlund, D., Gunnarsson, K., Malehmir, A., Högdahl, K., Bäckström, E., & Marsden, P. (2019). Magnetic characterisation of magnetite and hematite from the Blötberget apatite – iron oxide deposits (Bergslagen), south-central Sweden. *Canadian Journal of Earth Sciences*, *56*(9), 948–957. <https://doi.org/10.1139/cjes-2018-0183>
- Bobba, S., Carrara, S., Huisman, J., Mathieux, F., Pavel, C., & European Commission. (2020). Critical raw materials for strategic technologies and sectors in the EU: A foresight study. Publications Office of the European Union. <https://doi.org/10.2873/58081>
- Chen, P., Ilton, E. S., Wang, Z., Rosso, K. M., & Zhang, X. (2024). Global rare earth element resources: A concise review. *Applied Geochemistry*, *175*, 106158. <https://doi.org/10.1016/j.apgeochem.2024.106158>
- Connelly, N. G., Hartshorn, R. M., Damhus, T., & Hutton, A. T. (2005). *Nomenclature of inorganic chemistry: IUPAC recommendations 2005*. Royal Society of Chemistry.
- DMT (2015). *Mineral resource estimate for the Blötberget Iron Ore Project, Ludvika, Sweden* (Report No. C22-R-126). DMT Consulting Ltd, on behalf of Nordic Iron Ore AB.
- European Commission. (2023, March 16). *Critical raw materials: Ensuring secure and sustainable supply chains for EU's green and digital future*. European Commission. https://ec.europa.eu/commission/presscorner/detail/en/ip_23_1591

- European Commission. (2025, March 25). *COMMISSION DECISION of 25.3.2025 recognising certain critical raw material projects as Strategic Projects under Regulation (EU) 2024/1252 of the European Parliament and of the Council*. European Commission. https://single-market-economy.ec.europa.eu/sectors/raw-materials/areas-specific-interest/critical-raw-materials/strategic-projects-under-crma/selected-projects_en
- Frietsch, R., & Perdahl, J.-A. (1995). Rare earth elements in apatite and magnetite in Kiruna-type iron ores and some other iron ore types. *Ore Geology Reviews*, 9(6), 489–510. [https://doi.org/10.1016/0169-1368\(94\)00015-G](https://doi.org/10.1016/0169-1368(94)00015-G)
- Goldstein, J. I., Newbury, D. E., Michael, J. R., Ritchie, N. W. M., Scott, J. H. J., & Joy, D. C. (2017). *Scanning Electron Microscopy and X-Ray Microanalysis*. Springer.
- Goodenough, K. M., Schilling, J., Jonsson, E., Kalvig, P., Charles, N., Tuduri, J., Deady, E. A., Sadeghi, M., Schiellerup, H., Müller, A., Bertrand, G., Arvanitidis, N., Eliopoulos, D. G., Shaw, R. A., Thrane, K., & Keulen, N. (2016). Europe's rare earth element resource potential: An overview of REE metallogenetic provinces and their geodynamic setting. *Ore Geology Reviews*, 72, 838–856. <https://doi.org/10.1016/j.oregeorev.2015.09.019>
- Hansson, K. S. A., Högdahl, K., Bergqvist, M., Norell, J., Schött, J., Stansvik, E., & Häggström, C. (2024). Tungsten Concentrations in Mittersill Scheelite Ore Quantified with X-Ray Computed Tomography. *Mining, Metallurgy & Exploration*, 41(6), 2869–2876. <https://doi.org/10.1007/s42461-024-01103-1>
- Haque, N., Hughes, A., Lim, S., & Vernon, C. (2014). Rare Earth Elements: Overview of Mining, Mineralogy, Uses, Sustainability and Environmental Impact. *Resources*, 3(4), 614–635. <https://doi.org/10.3390/resources3040614>

- Jiao, JJ (2011). *Petrography and geochemistry of a section through the Blötberget apatite-iron oxide deposit, Bergslagen, south central Sweden*. [Unpublished MSc Thesis]. Uppsala University.
- Jonsson, E., Harlov, D. E., MaJka, J., Högdahl, K., & Persson-Nilsson, K. (2016). Fluorapatite-monazite-allanite relations in the Grängesberg apatite-iron oxide ore district, Bergslagen, Sweden. *American Mineralogist*, *101*(8), 1769–1782. <https://doi.org/10.2138/am-2016-5655>
- Jonsson, E., Troll, V. R., Högdahl, K., Harris, C., Weis, F., Nilsson, K. P., & Skelton, A. (2013). Magmatic origin of giant ‘Kiruna-type’ apatite-iron-oxide ores in Central Sweden. *Scientific Reports*, *3*(1), 1644. <https://doi.org/10.1038/srep01644>
- Jordens, A., Cheng, Y. P., & Waters, K. E. (2013). A review of the beneficiation of rare earth element bearing minerals. *Minerals Engineering*, *41*, 97–114. <https://doi.org/10.1016/j.mineng.2012.10.017>
- Kyle, J. R., & Ketcham, R. A. (2015). Application of high resolution X-ray computed tomography to mineral deposit origin, evaluation, and processing. *Ore Geology Reviews*, *65*, 821–839. <https://doi.org/10.1016/j.oregeorev.2014.09.034>
- Laperche, V., & Lemièrè, B. (2020). Possible Pitfalls in the Analysis of Minerals and Loose Materials by Portable XRF, and How to Overcome Them. *Minerals*, *11*(1), 33. <https://doi.org/10.3390/min11010033>
- Luth, S., Sahlström, F., Bergqvist, M., Hansson, A., Lynch, E. P., Sädbom, S., Jonsson, E., Andersson, S. S., & Arvanitidis, N. (2022). Combined X-Ray Computed Tomography and X-Ray Fluorescence Drill Core Scanning for 3-D Rock and Ore Characterization: Implications for the Lovisa Stratiform Zn-Pb Deposit and Its Structural Setting, Bergslagen, Sweden. *Economic Geology*, *117*(6), 1255–1273. <https://doi.org/10.5382/econgeo.4929>

- Mancheri, N. A. (2012). Chinese Monopoly in Rare Earth Elements: Supply–Demand and Industrial Applications. *China Report*, 48(4), 449–468.
<https://doi.org/10.1177/0009445512466621>
- Ripa, M., & Kübler, L. (2003). Apatite-bearing iron ores in the Bergslagen region of south-central Sweden. In M. Ripa (Ed.), *Economic geology research: Vol. 2, 2001–2002* (pp. 49–54). Sveriges geologiska undersökning. (Rapporter och meddelanden 113).
- Sovacool, B. K., Ali, S. H., Bazilian, M., Radley, B., Nemery, B., Okatz, J., & Mulvaney, D. (2020). Sustainable minerals and metals for a low-carbon future. *Science*, 367(6473), 30–33. <https://doi.org/10.1126/science.aaz6003>
- Stephens, M. B., & Jansson, N. F. (2020). Paleoproterozoic (1.9–1.8 Ga) syn-orogenic magmatism, sedimentation and mineralization in the Bergslagen lithotectonic unit, Svecokarelian orogen. In M. B. Stephens & J. Bergman Weihed (Eds.), *Sweden: Lithotectonic framework, tectonic evolution and mineral resources* (Geological Society, London, Memoirs, Vol. 50, pp. 155–206). Geological Society of London.
<https://doi.org/10.1144/M50-2017-40>
- Stephens, M. B., Ripa, M., Lundström, I., Persson, L., Bergman, T., Ahl, M., Wahlgren, C. H., Persson, P. O., & Wickström, L., (2009). Synthesis of the bedrock geology in the Bergslagen region, Fennoscandian shield, south-central Sweden. Sveriges Geologiska Undersökning *Ba 58*, 259 pp.
- Willemink, M. J., Persson, M., Pourmorteza, A., Pelc, N. J., & Fleischmann, D. (2018). Photon-counting CT: Technical Principles and Clinical Prospects. *Radiology*, 289(2), 293–312. <https://doi.org/10.1148/radiol.2018172656>

10. APPENDIX

A: Thin sections obtained from drill core BB-14-013

Table 1. BB-14-013 – Thin sections

Sample name	Depth (m)	Rock type	Petrography	SEM-EDS
B-13-522.5	522.5	Intermediate-metavolcanic	+	
B-13-525.7	525.7	Mafic-metavolcanics	+	
B-13-528.5	528.5	Intermediate-metavolcanic	+	
B-13-544A	544	Iron ore	+	
B-13-544B	544	Iron ore	+	+
B-13-544.2A	544.2	Iron ore	+	+
B-13-544.2B	544.2	Iron ore	+	
B-13-546A	546	Iron ore	+	+
B-13-546B	546	Iron ore	+	
B-13-548.3	548.3	Iron ore	+	
B-13-549.3	549.3	Iron ore	+	
B-13-549.5A	549.5	Iron ore	+	
B-13-549.5B	549.5	Iron ore	+	+
B-13-549.7	549.7	Iron ore	+	+
B-13-550.2	550.2	Iron ore	+	+
B-13-552.15	552.15	Iron ore	+	
B-13-557.9	557.9	Felsic-metavolcanics	+	
B-13-558.9	558.9	Mafic-metavolcanics	+	
B-13-560.2	560.2	Iron ore	+	+